Bioactive Materials 48 (2025) 100–117

Contents lists available at ScienceDirect

Bioactive Materials

journal homepage: www.keaipublishing.com/en/journals/bioactive-materials

Integrated biomimetic bioprinting of perichondrium with cartilage for auricle reconstruction

Litao Jia, Siyu Liu, Luosha Gu, Xiaomin Liu, Kexin Sun, Feiyang Chu, Jinshi Zeng, Wenshuai Liu, Haiyue Jiang **, Xia Liu *

Plastic Surgery Hospital, Chinese Academy of Medical Sciences and Peking Union Medical College, Beijing 100144, PR China

ARTICLE INFO

Keywords:
Three-dimensional bioprinting
Bioengineered perichondrium
Auricle regeneration
Biomimetic hierarchical structures
Tissue engineering

ABSTRACT

The construction and regeneration of tissue-engineered auricles are pacesetters in tissue engineering and have realized their first international clinical application. However, the unstable regeneration quality and insufficient mechanical strength have become significant obstacles impeding its clinical promotion. The perichondrium is indispensable for the nutritional and vascular supply of the underlying cartilage tissue, as well as for proper anatomical functioning and mechanical performance. This study presents a novel strategy for integrated construction of bioengineered perichondrium with bioprinted cartilage to enhance the regeneration quality and mechanical properties of tissue-engineered auricles. Simulating the anatomical structure of the native auricle designs a sandwich construction model containing bilateral perichondrium and intermediate cartilage, employing a photocrosslinkable acellular cartilage matrix and gelatin bionics matrix microenvironment, applying co-cultured auricular chondrocytes and adipose-derived stem cells creates functional cell populations, designing hatch patterns imitates microscopic arrangement structures, utilizing sacrificial materials forms interlaminar network traffic to enhance the tight connection between layers, and finally, assessing the regenerative quality of the constructs explores their feasibility and stability. The multi-level and multi-scale biomimetic construction strategy overcomes the technical limitation of the integrated construction of perichondrium-wrapped auricles and realizes biomimicry in morphology, structure, and biomechanics. Altogether, this study provides a technical reference for the hierarchical construction of complex tissues and promotes the clinical translation and application of engineered tissues or organs.

1. Introduction

Auricle defects caused by congenital diseases and acquired trauma are common in the clinic and seriously affect the physical and psychological health of patients [1,2]. Currently, the most effective treatment is auricle reconstruction based on autogenous cartilage carving [3,4]. However, auricle reconstruction has the disadvantages of high trauma, imprecise morphology, and many postoperative complications [5,6]. The rapid development in tissue engineering and regenerative medicine has provided promising strategies for auricle reconstruction [7,8]. Our team has successfully identified the first international clinical application of tissue-engineered auricles [9,10], revealing their great potential for clinical translation. However, the postoperative follow-up showed that the three-dimensional structure of tissue-engineered auricles gradually blurred, atrophied, deformed, and collapsed, resulting in unsatisfactory long-term clinical effects. Therefore, the unstable regeneration quality and insufficient mechanical strength of tissue-engineered auricles have limited their clinical application.

Macroscopic properties of the auricle are closely related to its matrix composition and microstructure [11,12]. The native auricle is lined by a stratified tissue called the perichondrium [13]. Unlike the underlying cartilage, perichondrium is indispensable for the nutritional and vascular supply of the underlying cartilage tissue and becomes invaluable to the maintenance of transplanted cartilage constructs [14]. Perichondrium might also be implicated in the metabolic regulation of cartilage, determining the proper functioning of chondrocytes, and inhibiting calcification. And the presence of the perichondrium layer is crucial to the flexibility of human auricular cartilage [15,16]. The

Peer review under the responsibility of KeAi Communications Co., Ltd.
* Corresponding author.
** Corresponding author.
E-mail addresses: jianghaiyue@psh.pumc.edu.cn (H. Jiang), liuxia@psh.pumc.edu.cn (X. Liu).

https://doi.org/10.1016/j.bioactmat.2025.02.011
Received 11 January 2025; Received in revised form 3 February 2025; Accepted 6 February 2025

structural role of perichondrium is essential for proper anatomical functioning and maintenance of the integrity of an engineered auricular graft. Cartilage-specific matrix components and microstructural features, together with the perichondrium wrapping, provide the auricle with good properties and strength. Therefore, simulating the matrix composition and microstructure of perichondrium-wrapped auricle through component and structural bionics may be a breakthrough in solving the unstable regeneration quality and deficiency in mechanical properties.

With the advancement of tissue engineering, it is necessary to construct bioengineered perichondrium because without this crucial tissue, the function of engineered cartilage for auricular reconstruction is incomplete and may not be suitable for long-term reconstructive goals. Meanwhile, the rapid development of three-dimensional bioprinting technology has enabled the combined construction of multiple cells and materials, providing technical support for the biomimetic construction of tissues and organs [17,18]. The central hypothesis of biofabrication is that the defined positioning of cells in a three-dimensional hierarchical manner aids the formation of complex tissue, where complexity is required to replicate the cellular microenvironment and communication pathways more reflective of the in vivo environment [19,20]. Since its advent, three-dimensional bioprinting technology has attracted much attention for the construction of auricular cartilage because of its remarkable advantages, such as personalization, accuracy, intelligence, and standardization [21,22]. However, integrated biomimetic construction of perichondrium-wrapped auricular cartilage tissue has not been reported. This study presents a novel strategy for integrated construction of bioengineered perichondrium with bioprinted cartilage with a hierarchical structure by mimicking the matrix composition and microstructure, and the multi-level and multi-scale biomimetic construction strategy overcomes the technical limitation of the integrated construction of perichondrium-wrapped auricles and realizes biomimicry in morphology, structure, and biomechanics.

2. Materials and methods

2.1. Materials and animals

Unless otherwise stated, all chemicals were of reagent grade and were supplied by Sigma–Aldrich (St. Louis, USA). New Zealand white rabbits (female, 2 months old). BALB/c nude mice (female, 8 weeks old) were purchased from the Beijing Longan Experimental Animal Breeding Center and Beijing Vital River Laboratory Animal Technology Co., Ltd. Animal experiments were approved by the Animal Care and Experiment Committee of the Plastic Surgery Hospital (Institute), Chinese Academy of Medical Sciences and Peking Union Medical College (Beijing, China).

2.2. Preparation of ECM-biomimetic hydrogel

Excess tissues and fascia on the surface of fresh auricular cartilage were removed to obtain cartilage pieces, which were then frozen and ground into cartilage powder after cooling with liquid nitrogen. The cartilage powder was sequentially treated with 0.5 % trypsin, a nuclease solution (containing 50 U/mL deoxyribonuclease and 1 U/mL ribonuclease A in 10 mM Tris-HCl, pH 7.5), 10 mM Tris-HCl (containing 10 U/ml aprotinin), and 1 % Triton X-100 solution for decellularization, as previously described [23,24]. Following the freeze-drying process, the decellularized cartilage powder was treated with 0.15 % collagenase solution, dialyzed against deionized water for 3 days, frozen, and lyophilized to obtain water-soluble acellular cartilage matrix (ACM). To prepare a photocrosslinkable hydrogel, water-soluble ACM was modified with methacrylic anhydride (MA) as previously described [25,26]. Briefly, 0.5 g of water-soluble ACM was dissolved in deionized water, and MA was added at a rate of 0.5 mL/min in an ice bath. The pH was maintained at 8–10 using 5 M NaOH, and the reaction continued overnight under constant stirring at 4 °C. After the reaction, the solution was neutralized with 1 M HCl and dialyzed using a 3500 D dialysis membrane in distilled water for 3 days, followed by freezing and lyophilization.

The ECM-biomimetic hydrogel was prepared 12 h before cell encapsulation, as previously reported [21]. Briefly, a certain amount of lyophilized ACMMA and gelatin methacrylate (GelMA) were weighed and fully dissolved in the culture medium to achieve a final concentration of 5 % each for ACMMA and GelMA. A certain amount of lithium acylphosphinate photoinitiator (LAP) was added, and the final concentration was maintained at 0.25 %. polyethylene oxide (PEO) powder (average Mw = 300,000), a pore-forming agent, was dissolved in this solution to obtain a final concentration of 1 % PEO solution. All the above hydrogel formulations were fully mixed by continuous stirring, sterilized with syringe filters (0.45 μm pore size), and stored in an incubator away from light. Finally, photocrosslinkable ACMMA-based hydrogels were induced by exposure to blue light (wavelength: 405 nm; light source: LED; intensity: 20 mW/cm^2; distance: 10 cm; exposure time: 30 s).

2.3. Isolation and cultivation of human ADSCs and auricular chondrocytes

Human adipose-derived stem cells (ADSCs) were isolated from discarded subcutaneous adipose tissue obtained by liposuction. Briefly, the collected adipose tissue was repeatedly washed with phosphate buffer saline (PBS) to remove connective tissue membranes and capillaries and then cut into chyliform. Adipose tissue was digested with 0.1 % collagenase type I to isolate ADSCs under gentle agitation at 37 °C, as previously described [27]. Then, the ADSCs were harvested, cultured, and expanded in a human mesenchymal stem cell medium (MesenCult™ Proliferation Kit, Stem Cell Technologies, Vancouver, BC, Canada) at 37 °C with 95 % humidity and 5 % CO_2. The ADSCs at the third passage were harvested and used for subsequent experiments after phenotypic identification using flow cytometry.

Under aseptic conditions, auricular cartilage was obtained from New Zealand white rabbits and minced into 1 mm^3 pieces. The cartilage pieces were washed with PBS and digested with 0.15 % collagenase type II to isolate chondrocytes under gentle agitation at 37 °C, as previously described [28]. Next, the chondrocytes were harvested, cultured, and expanded in high glucose Dulbecco's modified Eagle medium (DMEM, Gibco, Grand Island, NY) containing 10 % fetal bovine serum (FBS, Gibco, Grand Island, NY) and 1 % penicillin–streptomycin-neomycin antibiotic (PSN, Gibco, Grand Island, NY) at 37 °C with 95 % humidity and 5 % CO_2. After the second passage, the chondrocytes were harvested for further experiments.

2.4. Cell viability, proliferation, and tracking

After 1, 4, and 7 days of culture, the viability of cells encapsulated in hydrogels with different filling structures was evaluated using a Live and Dead Cell Viability Assay (Invitrogen, USA) following the manufacturer's instructions and examined using confocal fluorescence microscopy [29]. Five randomly selected visual fields per specimen were used to quantify cell viability using ImageJ software. In addition, DNA content was used to further assess cell proliferation capacity using a total DNA quantification assay (PicoGreen dsDNA assay, Invitrogen, USA), following the manufacturer's instructions, and measured using a fluorescence microplate reader.

To clarify the distribution of ADSCs and chondrocytes in the perichondrium and cartilage layers, different CellTracker™ fluorescent probes (Invitrogen, USA) were used to label the ADSCs and chondrocytes. Briefly, the ADSCs and chondrocytes were collected and prepared into single-cell suspensions, and the pre-warmed CellTracker™ Orange CMRA and CellTracker™ Green CMFDA working solutions were gently added, respectively. After incubation for 30 min under

appropriate growth conditions, the working solution was removed and then imaged using appropriate emission and excitation filters, according to the manufacturer's instructions [30].

2.5. FEA of different pattern-filling constructs

Samples were obtained from three constructs with different filling patterns using three-dimensional bioprinting. The three constructs were 10 mm in length, 5 mm in width, and 2.5 mm in height. The load-bearing capacities of the three different constructs were simulated using FEA, as previously reported [31]. Briefly, the modeling parameters and parametric equations were determined according to the parameters of the three different printing models, and the CAD models of the line, wave, and honeycomb patterns were established using Creo 5.0. Then, the three different models were meshed using Hypermesh 2020 software (Altair Engineering Inc., USA) to establish the simulation model for the FEA. Next, the three structures were subjected to compression analysis using Abaqus/Standard 2019 software (Dassault Systems Simulia Corp., Providence, RI, USA). Downward compression (0.5 mm) was applied to the platen to simulate 10 % compressive deformation. The Young's modulus and Poisson's ratio used for the FEA were obtained in advance from the mechanical tests of the corresponding units. Considering the nonlinearity of the geometric deformation, the theory of large-deformation analysis of linear elastic materials was adopted to calculate and analyze the displacement deformation, stress distribution, and load-bearing capacity of the three constructs.

2.6. Bioprinting of the cell-laden constructs with different pattern-filling

A three-dimensional digital model of the cuboid shape with dimensions of 10 mm × 5 mm × 2.5 mm was constructed using Perfactory RP software (Version 3.2). After performing the layering process (layer height: 320 μm, number of layers: 8 layers), the three-dimensional digital model was exported to Visual Machines software (Version 2.10) to design the internal structure. According to the structural characteristics of the native auricle, three types of internal structures were designed, including line-pattern, wave-pattern, and honeycomb-pattern, and detailed parameters, such as strand spacing, period, and amplitude, were adjusted (Table S1). Auricular chondrocytes were collected and mixed with the ECM-biomimetic hydrogel formulation precursors at a concentration of 2.5×10^7 cells/mL. After temperature stabilization, bioprinting was performed using a three-dimensional Bioplotter (Envision TEC, Germany) with the printing parameters listed in Table S1. During the bioprinting process, photocrosslinkable bioink was solidified under continuous irradiation from a blue light source. Finally, cell-laden constructs with different filling patterns were constructed and cultured in a medium that was then transplanted subcutaneously into nude mice to observe cartilage formation in vivo.

2.7. Bioprinting of the sandwich constructs with biomimetic hierarchical structures

According to the anatomical characteristics of the perichondrium-wrapped auricle, a sandwich construction with biomimetic hierarchical structures was designed, which included the perichondrium on both sides and the cartilage in the middle. In addition, two bio-ink formulations and two construction patterns were designed based on the ECM composition, functional cell types, and microstructural characteristics of the perichondrium and cartilage. Bio-ink formulation precursors were prepared as described above (a) Perichondrium-bioink: 10 % GelMA, 1 % PEO, 0.25 % LAP, 5.0×10^6 cells/mL ADSCs co-cultured with 2.0×10^7 cells/mL chondrocytes; (b) Cartilage-bioink: 5 % ACMMA, 5 % GelMA, 1 % PEO, 0.25 % LAP, and 2.5×10^7 cells/mL chondrocytes. The three-dimensional digital model of the sandwich structure with 8.4 mm × 8.4 mm × 2.0 mm in dimensions was constructed, and the detailed printing parameters are shown in Table S2. The digital model was sliced into six layers, where the first and sixth layers were designed as perichondrium layers using perichondrium bio-ink and filled with a wave pattern, whereas the middle four layers were designed as cartilage using cartilage bioink and filled with a honeycomb pattern. The contours of the six layers were printed using perichondrium bioink to ensure that the regenerated cartilage was wrapped by the regenerated perichondrium.

2.8. Bioprinting of the auricular constructs with biomimetic hierarchical structures

Three-dimensional digital models of the human auricle were reconstructed and prepared using three-dimensional laser scanning and a CAD system (CAD, 3DPRO Technology Co., Ltd., Shanghai, China), as previously described [32,33]. The bioprinting process of the auricular digital models consisted of two patterns: (a) the first and last layers, as well as the contours of all layers, were designed as perichondrium layers, using perichondrium bioink filled with a wave pattern; (b) the middle 21 layers were designed as cartilage, using cartilage bioink filled with a honeycomb pattern; the detailed printing parameters are shown in Table S3. According to the designed biomimetic hierarchical structures, perichondrium-wrapped auricular substitutes were constructed integrally based on the layer-by-layer deposition printing method with multiple nozzles by applying the optimized bioink formulation, cell type, density, and printing parameters. After bioprinting and crosslinking, the perichondrium-wrapped auricular constructs were cultured and subcutaneously transplanted into nude mice for regeneration to form auricles with biomimetic hierarchical structures.

2.9. Three-dimensional reconstruction and morphological analysis

After 24 weeks of culture in vivo, the regenerated perichondrium-wrapped auricular cartilage was collected and scanned using a Quantum GX Micro Computed Tomography (micro-CT) Imaging System (PerkinElmer, USA) to obtain DICOM files. The DICOM files were imported into Mimics Medical software (version 21.0, Materialise, Belgium) for three-dimensional reconstruction to generate STL files. The three-dimensional reconstruction model files, as well as the initial digital model files, were inputted into the Geomagic Control software (version 2015), setting the initial digital model as the *reference* and the three-dimensional reconstruction model as the *test*. After precise fitting and adequate alignment, the morphological similarity of the two models was analyzed using a three-dimensional deviation comparison and displayed as a deviation chromatogram, as previously reported [34,35].

2.10. Histological, immunohistochemical, and immunofluorescence analysis

Specimens from different groups were collected and subjected to histological and immunohistochemical analyses, as described previously [28]. Briefly, all samples were fixed in 4 % paraformaldehyde, embedded in paraffin, and sectioned into 4 μm-thick slices. The tissue sections were then stained with hematoxylin-eosin, Safranine O-fast green, Masson's trichrome, elastic van Gieson, and picrosirius red to evaluate their histological structure and cartilage-specific ECM deposition in the regenerated tissue. The expression of type I and type II collagen was detected using monoclonal antibodies against collagen I (ab138492, 1:500; Abcam, Cambridge, UK) and collagen II (MS-306-P1, 1:200; Invitrogen, USA), followed by incubation with the corresponding horseradish peroxidase-conjugated secondary antibodies. All antibodies were diluted using antibody diluents (Invitrogen, USA) and stained with diaminobenzidine tetrahydrochloride (DAB, Dako, Denmark).

To determine the primary cellular origin of the regenerated perichondrium-wrapped cartilage tissue, tissue sections were incubated with a monoclonal antibody against Lamin A/C (ab8984, 1:200; Abcam, Cambridge, UK), a human nuclear envelope marker that specifically identifies full-length Lamin A/C in human cells [36]. After incubation

with a horseradish peroxidase-conjugated secondary antibody, the signals were amplified and detected using Tyramide Signal Amplification (TSA) Plus Cyanine 3 (Cy3). The primary antibodies for type I collagen, type II collagen, and the corresponding horseradish peroxidase-conjugated secondary antibodies were incubated sequentially according to the steps described above. Hybridization signals were amplified and visualized using TSA plus Cyanine 5 (Cy5) for collagen I and TSA Plus fluorescein for collagen II. Finally, the nuclei were counterstained with 4, 6-diamino-2-phenylindole, and fluorescence images were collected using a Leica fluorescence microscope (Leica DM IRB).

2.11. Visualization of collagen fiber orientation and alignment quantification

Tissue sections stained with picrosirius red were imaged using PLM (BX-45; Olympus, Hamburg, Germany) to visualize collagen fiber orientation as previously described [37]. Both native and engineered tissues were divided into perichondrium and cartilage zones. Quantification of the average fiber orientation and dispersion was performed using the directionality plugin in ImageJ software, and fiber coherency and color maps were determined using OrientationJ, an ImageJ plugin developed in-house based on structure tensors [38]. The structure sensors are matrix representatives of the partial derivatives, and the OrientationJ plugin was used to evaluate the local orientation and isotropic properties (coherency and energy) of each pixel of the image.

2.12. Biochemical quantification and biomechanical analysis

Specimens from different groups were collected and minced for relevant biochemical evaluations, including DNA, glycosaminoglycan (GAG), and total collagen content, according to previously established protocols [39]. Briefly, DNA, GAG, and total collagen contents were measured using Quant-iT™ PicoGreen® dsDNA assay, Dimethylmethylene Blue assay, and Hydroxyproline assay kit, respectively. The expression of cartilage-related genes, such as aggrecan, collagen type II alpha 1, collagen type IX alpha 1, elastin, and SRY-box transcription factor IX; and perichondrium-related genes, such as collagen type I alpha 1, collagen type III alpha 1, fibroblast activation protein alpha, fibrillin 1, and actin alpha 2 smooth muscle, as well as the expression of proliferation and vascular-related genes, such as fibroblast growth factor 1, transforming growth factor beta 1, insulin-like growth factor 1, vascular endothelial growth factor A, and von Willebrand factor were analyzed quantitatively with the SYBR Green using LightCycler® 96 Real-Time PCR system (Roche Ltd) according to a previously established method. Forward and reverse primer sequences were designed based on published gene sequences from the National Center for Biotechnology Information and PubMed (Tables S4 and S5). The relative expression levels for each gene were normalized with glyceraldehyde phosphate dehydrogenase and analyzed using the $2^{-\Delta\Delta CT}$ method.

Biomechanical performance was analyzed using a biomechanical analyzer (Instron-5967, Canton, MA, USA). All specimens were refined into cylindrical and dumbbell shapes for the compressive, tensile, and flexural tests. Compression tests were performed at a constant strain rate of 1 mm/min until 80 % of maximum deformation was achieved, tensile tests were performed at a strain rate of 2 mm/min until failure, flexural tests were performed at a strain rate of 2 mm/min until 10 % deformation, and Young's modulus was calculated based on the slope of the stress-strain curve. A humidifier was used to maintain ambient humidity during all the tests.

2.13. Transcriptome analysis of native and engineered tissues

Native and engineered auricular tissues were carefully separated into perichondrium and cartilage regions, which were collected separately and then used for transcriptome analysis. Briefly, samples from all groups were ground in liquid nitrogen, and total RNA was isolated and extracted using the TRIzol reagent (Invitrogen, USA) according to the manufacturer's instructions. The total amount and integrity of RNA were assessed using the RNA Nano 6000 Assay Kit of the Bioanalyzer 2100 system (Agilent Technologies, CA, USA). Thereafter, mRNA was purified from total RNA using poly T oligo-attached magnetic beads and reverse transcribed into cDNA fragments. RNA-seq libraries were obtained by purifying the fragments and PCR products using the AMPure XP system (Beckman Coulter, Beverly, USA). After identification using the Agilent 2100 bioanalyzer, the libraries were subjected to paired-end sequencing using the Illumina NovaSeq 6000 (Illumina, USA) according to the manufacturer's protocol. Mapping and enrichment analyses were performed as previously described [40]. Briefly, the index of the reference genome was built using Hisat2 (v2.0.5), and paired-end clean reads were aligned to the reference genome using Hisat2 (v2.0.5). Differential gene expression and enrichment analyses were performed using Gene Ontology (GO), the Kyoto Encyclopedia of Genes and Genomes (KEGG), and Gene Set Enrichment Analysis (GSEA) in the R software. The resulting *P*-values were adjusted to control for the false discovery rate. *P*-values <0.05 and $|\log_2(\text{fold change})| > 1$ were set as the threshold for significantly differential expression or differential enrichment. Protein-protein interactions (PPI) analysis of differentially expressed genes was based on the STRING database, which is available for known and predicted Protein-Protein Interactions.

2.14. Statistical analysis

All quantitative data were collected from at least five replicate experiments and are expressed as means ± standard deviation. After testing for normal distribution, differences between the groups were evaluated using the student's t-test or one-way analysis of variance using GraphPad Prism 8.0 software, and a *P*-value <0.05 was considered statistically significant.

3. Results

3.1. Characterization of native auricle and different pattern-filling constructs

The normal anatomical structure and histological characteristics of a native auricle are shown in Fig. 1A. Gross view showed that a native auricle is mainly divided into three layers consisting of bilateral perichondrium and middle cartilage. Histologically, perichondrium on both sides consists of several layers of fibrous tissue, and the extracellular matrix is composed mainly of type I collagen, with no expression of type II collagen. Collagen fibers are arranged in parallel and scattered throughout the blood vessels. In the area close to the cartilage, the fibers anchored and grew into the cartilaginous matrix, which was tightly bound to the cartilage. Chondrocytes in the cartilage exist in the cartilage lacunae. The ECM is mainly composed of type II collagen and elastin, similar to the honeycomb reticular arrangement. We speculate that the parallel arrangement of collagen fibers of the perichondrium bilayers improves tensile strength, whereas the honeycomb reticular structure in the cartilage improves the compressive strength of the auricle, which was confirmed by the results of biomechanical tests. As shown in Fig. 1B, the compressive and tensile moduli of the cartilage perichondrium-wrapped auricle were significantly higher than those without the perichondrium. When the cartilage tissue is ruptured by an external force, preserving the perichondrium can effectively maintain the integrity of the cartilage tissue. Therefore, the ECM components and structural characteristics, together with the wrapping by the perichondrium, provide the auricle with good mechanical properties.

Therefore, the wave and honeycomb structures were designed by simulating the fiber arrangement characteristics of the perichondrium and cartilage and were compared with the conventional line pattern to explore the effects of the three different internal structures on the mechanical properties. First, 10 % compressive deformation was simulated

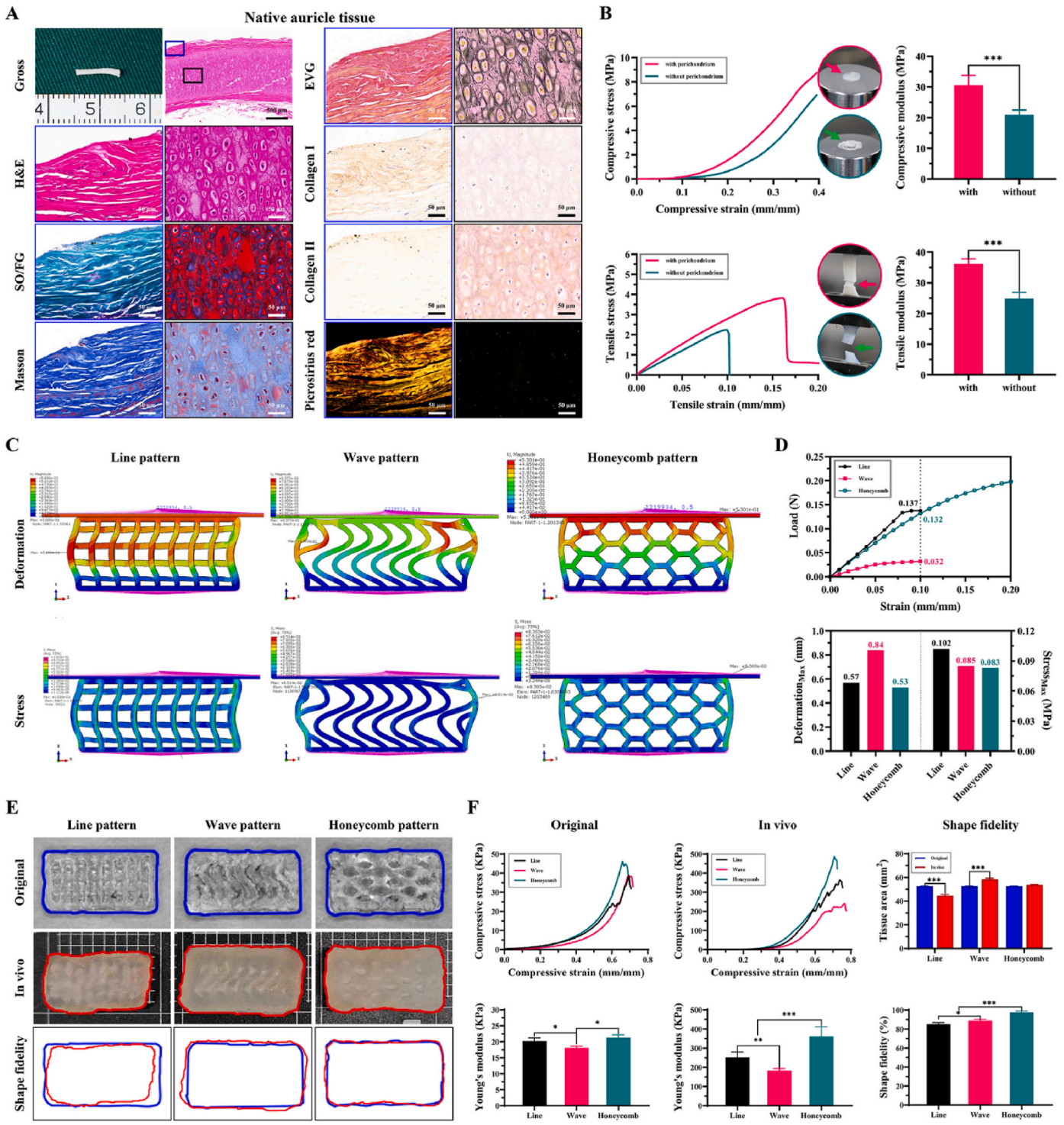

Fig. 1. Characterization of native auricle and different pattern-filling constructs. (A) Gross view and histology of native perichondrium-wrapped auricle. (B) Compressive and tensile properties of native auricular cartilage with and without perichondrium. (C) Finite element analysis of different pattern-filling constructs (line, wave, and honeycomb). (D) Simulated compression curves, deformations, and stresses of different pattern-filling constructs. (E) Original bioprinted morphology, in vivo regenerated morphology, and shape fidelity of different pattern-filling constructs. (F) Compressive stress-strain curves, Young's modulus, and shape fidelity of the original bioprinted constructs and in vivo regenerated tissues of different pattern fillings. $^{*}P < 0.05$. $^{**}P < 0.01$. $^{***}P < 0.001$.

using finite element analysis (FEA), and the global and local displacement deformation, stress distribution, and load-bearing capacity were analyzed (Fig. 1C). Statistically, the deformation of the wave pattern was the largest, and beyond 5 % strain, the load capacity no longer changed linearly (Fig. 1D). The deformation and stress of the line and honeycomb patterns were similar at 10 % compressive deformation; however, the line pattern showed a yield point beyond 8 % strain in which the deformation and load capacity no longer changed linearly, and the bearing capacity began to weaken. The line pattern has the highest local stress distribution, indicating that the internal stress distribution was high, the ability to disperse the stress was poor, and the internal structure was at risk of fracture. In addition, the line pattern was

at risk of lateral deformation, indicating structural instability. The honeycomb pattern was linear at 10 % compressive deformation, and after further testing at approximately 20 % strain, it was still approximately linear with no yield point, indicating that the bearing capacity could be continuously maintained. The local stress distribution and deformation of the honeycomb pattern were the smallest, indicating that it had a strong ability to dissipate stress and that the internal structure was not easily fractured. In addition, there was no risk of lateral displacement, indicating that the overall structure was stable.

Cell-laden constructs with line, wave, and honeycomb patterns were successfully developed using three-dimensional bioprinting technology, and real-time imaging revealed that the constructs have different internal structures (Fig. S1). Due to layer accumulation, the morphological outline and internal structure of the constructs became visible. After bioprinting, a general view (Figs. S2A–C) of the constructs showed that they were morphologically stable and were not significantly different regarding volume, reflecting the accuracy and stability of the three-dimensional bioprinting technology. With the prolongation of culture time in vitro, the pores of the constructs gradually decreased in size and slightly increased in thickness, and the internal structure was still visible on day 7. In addition, to eliminate the interference of cell number and nutrient exchange caused by the filling ratio and porosity, printing parameters were calculated and adjusted to ensure that the constructs had similar filling ratios, void fractions, and wet weights ($P > 0.05$, Figure S2 D–F). However, it is worth noting that the thickness of the line pattern, as well as the failure strain and stress, were significantly lower than those of the wave and honeycomb patterns ($P < 0.05$, Figure S2 G–I), which may be due to the deposition angle of 0°/90° in the line pattern. During layer-by-layer accumulation, the lack of complete support in the line pattern resulted in a certain degree of structural collapse. Because there was no transformation in the deposition angle in the wave and honeycomb patterns, complete support with a stable overall structure was achieved during layer-by-layer accumulation.

The internal structure of the scaffold not only affects the mechanical properties and stability of the constructs but may also influence cell activity and tissue formation. First of all, the effects of bioprinting cell-laden constructs with different patterns on cell activity were evaluated using Live/Dead staining. As shown in Fig. S3, the constructs with different patterns maintained good structure and morphology, the cells were evenly distributed with good viability, and there was no statistically significant difference in cell survival. With the extension of the culture time, the cells grew well with a gradual increase in the number of living cells, indicating that the constructs with different structures had good biocompatibility and were suitable for three-dimensional culture. In addition, there was a higher density of living cells around the edges and pores, which may be related to more frequent nutrient exchange in these areas. Next, the effects of bioprinted constructs with different structures on cartilage regeneration were evaluated by in vivo experiments. As shown in Fig. 1E and Figs. S4A–C, the scaffolds with different patterns were uniform in size and with a clear structure before implantation. After 4 weeks in vivo, all the constructs of the different groups formed porcelain white cartilage-like tissue. Regarding morphological maintenance, the constructs with line patterns collapsed and shrank obviously, with a significantly smaller surface area and decreased thickness. The volume of the constructs with wave patterns showed no obvious change, but there was some deformation with a larger surface area and thinner thickness. The shape fidelity of the constructs with honeycomb patterns was the best, with no obvious deformation. In addition, in terms of mechanical properties, the Young's modulus and failure stress of the constructs with honeycomb patterns were also significantly higher than those with the line pattern and wave patterns groups (Fig. 1F, Figure S4D and E), which also confirmed the above theoretical conjecture and the results of the FEA, and further demonstrated that the honeycomb structure helped improve the compressive resistance and overall stability. Histological and biochemical quantitative results showed that there were no statistically significant differences among the different groups (Figs. S4F–H). Mature cartilage lacunae, cartilage-specific matrix deposition, and neocartilage-like tissue formation could be seen in all the constructs with different patterns (Fig. S5), indicating that these three different internal structures had no significant effect on the regeneration quality of the cartilage tissue under the condition of a consistent scaffold filling ratio and void fraction.

3.2. Bioprinting and regeneration of sandwich constructs with hierarchical structures

To better simulate the microstructural arrangement characteristics of the natural auricle, an integrated layered construction strategy was proposed based on the concept of a sandwich structure. As shown in Fig. 2A, wave patterns arranged in parallel on the top and bottom sides were printed to simulate the perichondrium structure. Honeycomb patterns were printed in the middle area to simulate the cartilage structure, and sandwich constructs wrapped with perichondrium were integrated using layer-by-layer accumulation. In addition, by simulating the characteristics of collagen fibers protruding from the perichondrium and anchored in the cartilage matrix, PEO was used to form network communication, which not only provides space for cells to proliferate and secrete matrix but also promotes the tight connection between the perichondrium and cartilage. After realizing the integrated fabrication of perichondrium-wrapped cartilage constructs, cell distribution and behavior in the perichondrium and cartilage were evaluated. As shown in Fig. 2B, Live/Dead staining showed good cell growth (green fluorescence) with few dead cells (red fluorescence) and wave and honeycomb patterns with well-maintained morphology. There was no significant difference in cell viability before and after bioprinting (Fig. 2C), demonstrating that the bioprinting process did not adversely affect cell survival. Over time, the DNA content of the cells in each group gradually increased, indicating a significant increase in the number of cells. Notably, the proliferation rates of cells with the wave and honeycomb patterns were significantly better than those before printing. We speculate that this may be due to the pore structure formed after printing, which is conducive to the exchange of nutrients and promotes cell proliferation.

To clarify the distribution of different functional cells in the perichondrium and cartilage, chondrocytes and ADSCs were labeled and traced using different fluorescence probes: green for chondrocytes and orange for ADSCs (Fig. 2D). The cross-sectional view of the sandwich constructs showed that the functional cell population of the perichondrium (ADSCs co-cultured with chondrocytes) was distributed on the upper and lower sides as well as the border area, whereas the functional cell group of the cartilage (chondrocytes) was distributed in the middle area. In addition, the bilateral layer of the perichondrium with wave patterns comprised perichondrium functional cells, the intermediate area with honeycomb patterns comprised cartilage functional cells, and the border area comprised perichondrium functional cells, indicating a successful construction of perichondrium-wrapped cartilage tissue. In other words, through the orientation and precise placement of the bio-ink, the macrostructure and geometric configuration of the cell population can be controlled to achieve structural biomimicry. Simultaneously, by adjusting the ratio of seed cells to biomaterials in the perichondrium and cartilage, biomimicry of functional cells and matrix components can be realized, thereby realizing the integrated biomimetic construction of perichondrium-wrapped cartilage tissue.

After three months of transplantation into nude mice, a cross-sectional view of the sandwich constructs showed the delamination of the engineered perichondrium (Eperichondrium) and cartilage (Ecartilage) compared with the homogeneous cartilage constructs (Figure S6 and Figure S7). Histological analysis showed that the Eperichondrium on both sides had collagen fibers arranged in parallel with positive straining for collagen I. The middle-Ecartilage showed mature cartilage lacunae, positive staining for glycosaminoglycans, and deposition of

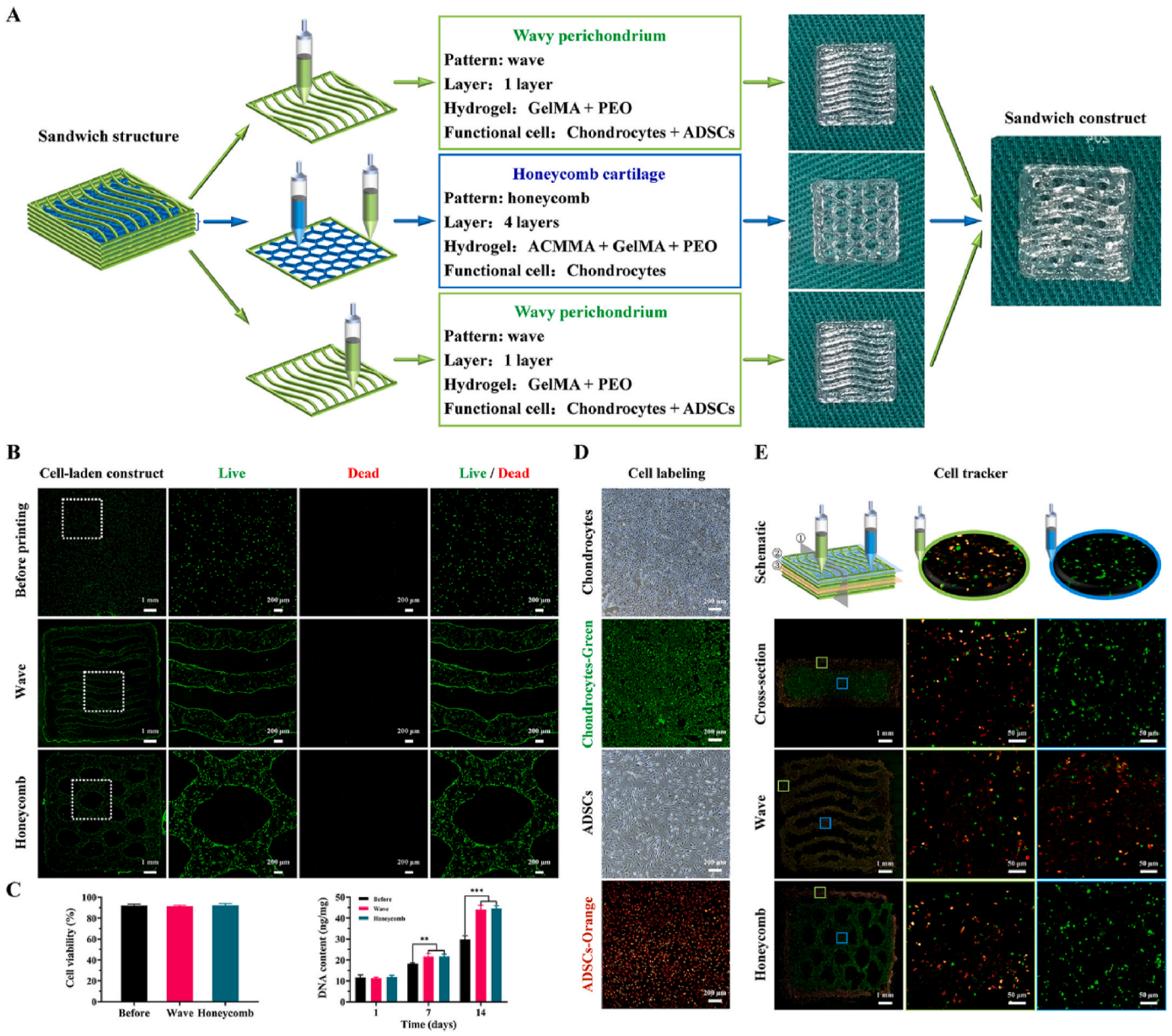

Fig. 2. Bioprinting of cell-laden sandwich constructs with hierarchical structures. (A) Schematic illustration of bioprinting strategy for the sandwich structure and the gross view of the bioprinted cell-laden sandwich constructs. (B) Live/dead staining of the before printing, wave pattern, and honeycomb pattern constructs (green fluorescence and red fluorescence representing live cells and dead cells, respectively). (C) Cell viability and DNA content of the before printing, wave pattern, and honeycomb pattern constructs. (D) Chondrocytes and ADSCs were labeled with green fluorescence and orange fluorescence, respectively. (E) Cell tracking of chondrocytes and ADSCs in sandwich constructs with biomimetic hierarchical structures. $^{**}P < 0.01$. $^{***}P < 0.001$.

collagen II and elastin. Histologically, the different layers of the sandwich constructs showed that the Eperichondrium and Ecartilage were arranged in wave and honeycomb patterns, respectively, with good shape retention and a clear internal structure (Figure S8 and Figure S9). The perichondrium with a wave pattern had an alternating arrangement of fibers and cartilage, with collagen I interspersed with collagen II in a parallel arrangement. The inner filling area of the cartilage with a honeycomb pattern was a mature cartilage-like tissue with mature cartilage lacunae and abundant cartilage-specific matrix deposition, whereas the border area was a parallel arrangement of fibers with collagen I. In addition, under polarized light irradiation (PLM) after Sirius Red staining, the Eperichondrium showed strong yellow or red birefringence, and the fibers were closely arranged, while the Ecartilage showed weak green refraction and loose reticular distribution, further indicating that the Eperichondrium and Ecartilage were dominated by collagen I and II, respectively. These results provide preliminary evidence of the successful regeneration of sandwich constructs and a hierarchical structure similar to that of native auricle tissue. Notably, possibly due to the successful construction of a biomimetic hierarchical structure, the compressive, tensile, and bending moduli of the regenerated tissue were significantly higher in the perichondrium-wrapped grafts (Fig. S10), indicating that the perichondrium-wrapped cartilage tissue fused into a monolithic structure and was able to withstand greater external forces. This further validates the theory that cartilage-specific matrix components, microstructural features, and perichondrium wrapping impart good mechanical properties to Ecartilage.

3.3. Bioprinting and regeneration of auricular cartilage with hierarchical structures

Furthermore, through the bioprinting of the aforementioned sandwich structure, perichondrium-wrapped auricles with biomimetic hierarchical structures were fabricated based on the hierarchical structure, matrix components, functional cells, and arrangement characteristics of the native auricle. After slicing the three-dimensional digital model of the human auricle (14.0 × 24.0 × 7.5 mm), prepared by three-dimensional laser scanning and computer-aided design (CAD) technology, the outer shell and inter-core were designed as the perichondrium and cartilage layers, respectively (Fig. 3A). Then, the perichondrium and cartilage layers were bioprinted with the corresponding bioink to form wave and honeycomb patterns, respectively (Fig. 3B), and a perichondrium-wrapped auricle was fabricated through layer-by-layer accumulation (Fig. 3C–Movie S1). After 7 days of culturing, Live/Dead staining results showed that the cells in the constructs had good viability and that the perichondrium and cartilage layers retained their wave and honeycomb patterns, respectively (Fig. 3D).

Then, the perichondrium-wrapped auricles were transplanted subcutaneously into nude mice to investigate the regeneration quality in vivo. As shown in Fig. 3E, the auricle constructs on the backs of the nude mice maintained their original auricle shape after 24 weeks. The gross view after harvesting showed a porcelain-white cartilage-like tissue that maintained its original size, defining the auricle structure with good elastic properties because when external forces were removed, it quickly

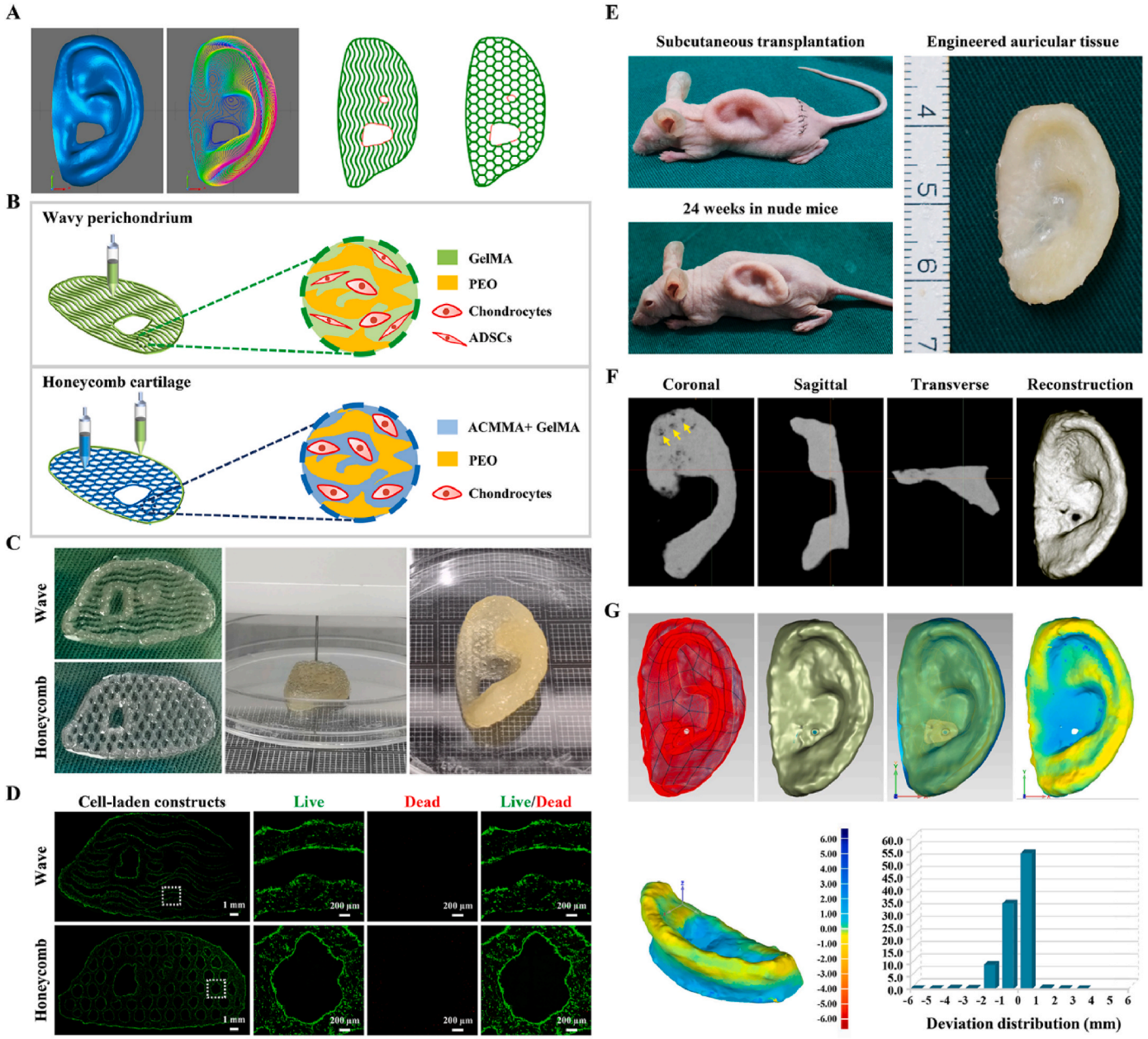

Fig. 3. Bioprinting and regeneration of perichondrium-wrapped auricles with hierarchical structures. (A) The three-dimensional digital model of human auricle and schematic diagram of the internal patterns. (B) Schematic illustration of the layered bioprinting strategy for the perichondrium-wrapped auricle. (C) Integrated bioprinting process of perichondrium-wrapped auricular constructs. (D) Live/Dead staining of bioprinted perichondrium-wrapped auricular constructs. (E) Gross view of the regenerated perichondrium-wrapped auricular cartilage at 24 weeks in vivo. (F) Micro-CT scan images and three-dimensional reconstruction images of the engineered perichondrium-wrapped auricular cartilage. (Yellow arrows: preserved honeycomb structure of the cartilage layer) (G) Three-dimensional deviation comparison of the engineered perichondrium-wrapped auricular cartilage.

returned to its original state without being destroyed (Movie S2). Ideally, the shape and size of engineered auricle substitutes should match the original digital model. Tomographic scanning of the regenerated auricle substitutes was performed using micro-CT, showing well-defined contours in all sections (Fig. 3F–Movie S3–5), whereas the honeycomb structure of the cartilaginous layer was preserved in the coronal sections (yellow arrows). The densities of the perichondrium and cartilage were too similar to distinguish and segment the scanned images. After three-dimensional reconstruction, the engineered auricle substitutes were fitted and aligned with the original digital model, and a

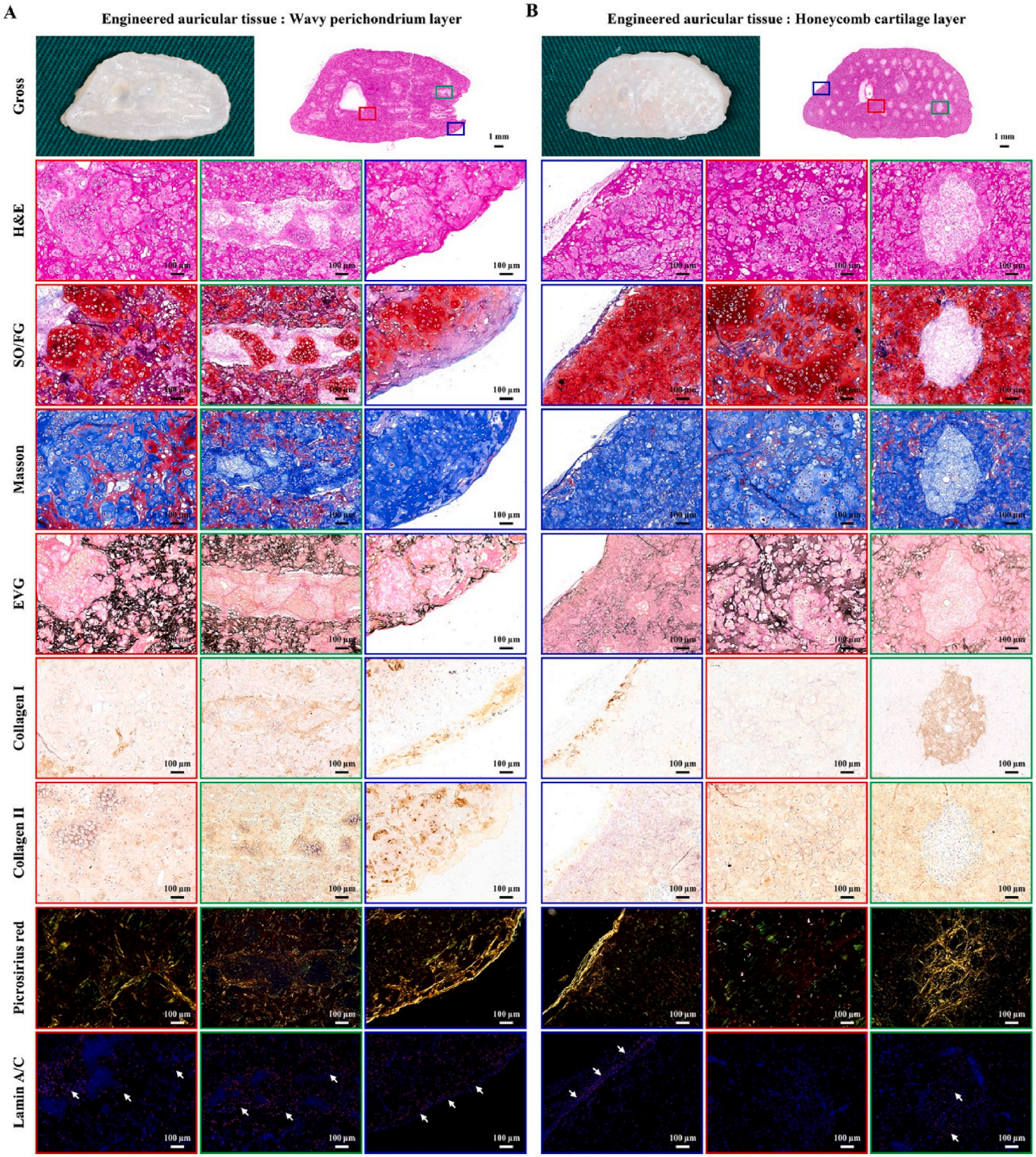

Fig. 4. Regenerative quality of engineered perichondrium-wrapped auricular tissue with hierarchical structures. Gross view and histological staining (H&E, SO/FG, Masson, EVG, Collagen I, Collagen II, Picrosirius Red, and Lamin A/C) of (A) Wavy perichondrium layer and (B) Honeycomb cartilage layer of the engineered perichondrium-wrapped auricular tissue at 24 weeks in vivo. (White arrows: positive staining of human nuclei with red fluorescence).

three-dimensional deviation comparison was performed to quantify morphological similarity (Movie S6 and S7). The morphological similarity was measured using a deviation chromatogram, and the deviation reached 89.39 ± 1.86 % in the range of ±1 mm (Fig. 3G), indicating that the original auricle morphology was essentially maintained after 24 weeks of culture in vivo.

After successfully regenerating the perichondrium-wrapped auricle, it is necessary to clarify the formation quality of each layer. As shown in Fig. 4, the coronal sections of the perichondrium and cartilage layers exhibited wave and honeycomb patterns, respectively, with well-maintained shapes and clear internal structures. Histologically, the perichondrium layer with a wave pattern showed an alternating arrangement of fibrous and cartilaginous tissues, and collagen I was interspersed with collagen II in a parallel arrangement. The inner honeycomb-patterned area of the honeycomb cartilage layer was mature cartilage-like tissue with mature cartilage lacunae and a large number of cartilage-specific matrix depositions, whereas the border area showed a parallel arrangement of fibrous tissue with collagen I. Similarly, the perichondrium region showed strong yellow or red birefringence, and the fibers were tightly arranged, whereas the cartilage region showed weak green refraction and reticular distribution, further indicating that the perichondrium and cartilage contained type I and type II collagen, respectively. Consistent with the histological results, the expression of chondrogenesis and fibrogenesis related proteins (Fig. S11) indicated that the engineered cartilage exhibited high expression of chondrogenesis-related proteins, while the engineered perichondrium demonstrated high expression of fibrogenesis-related proteins. The engineered tissues exhibited comparable protein expression trends and approached the protein expression levels observed in native tissues.

To further identify the distribution and origin of the functional cells in the Eperichondrium and Ecartilage, Lamin A/C (a human nuclear envelope marker) was used to identify human ADSCs in the constructs. Immunofluorescence analysis showed that the transplanted human ADSCs survived for a long time and maintained their phenotype. Most ADSCs remained in the perichondrium, while some migrated to the cartilage, further suggesting the successful establishment of interlamellar network connections. Positive areas of the human nucleus in the perichondrium or cartilage were consistent with the deposited areas of collagen I, indicating that type I collagen fibers are likely to be differentiated and secreted by human ADSCs. Additionally, the pores in the honeycomb cartilage showed the deposition of type I collagen, and human nucleus staining was positive, suggesting that it probably migrated and was secreted by human ADSCs in the adjacent perichondrium, confirming a successful establishment of interlamellar network traffic, which contributes to the promotion of a tight connection between the perichondrium and cartilage.

3.4. Visualization and quantitative analysis of collagen fiber orientation

Successfully engineered substitutes require biomimetic compositions, architectures, and mechanical properties akin to those of native tissue. The scanning electron microscopic (SEM) images in Fig. 5A and B demonstrate that the regenerated tissue possessed a hierarchical structure and collagen fiber network resembling that of native tissue. Specifically, the collagen fibers in the perichondrium were arranged in parallel, while the chondrocytes in the cartilage were uniformly distributed within a matrix, resembling a honeycomb reticular structure. The overall performance of biological tissues is largely determined by the orientation and distribution of collagen fibrils. Thus, PLM was utilized to assess the histological degree of collagen fibers, and the predominant angles of collagen fiber orientation were analyzed in both the perichondrium and cartilage. Notably, the color and intensity of collagen birefringence are influenced by the alignment of collagen fibrils, packing density, and fibril diameter. As depicted in Fig. 5C and D, densely packed and highly aligned collagen fibrils in the perichondrium regions exhibited yellow birefringence, whereas collagen fibers radiating in the cartilage regions displayed green birefringence. These characteristics were solely observed in normal mature tissue, suggesting a similarity between the engineered tissue and mature native tissue. Furthermore, the Eperichondrium area exhibited not only parallel yellow birefringence but also radially arranged green birefringence, possibly due to the presence of a functional cell population containing chondrocytes in the perichondrium, which produced cartilage-specific type II collagen fibers.

To visualize the alignment of collagen fibers in native and engineered tissues, images were post-processed using the OrientationJ plugin in ImageJ to create a color survey map of fibril orientation as well as their coherency and orientation. Color wheels were provided to show how hue corresponds to fiber directionality; that is, red/pink corresponds to fibers that aligned towards 90°, and cyan/blue corresponds to fibers that were oriented at 0°. The collagen fibers in the perichondrium were mainly cyan or blue, indicating that the fibers were aligned parallel to 0°. The collagen fibers in the cartilage exhibited a variety of colors, indicating that the fibers were oriented in all directions. Meanwhile, the high and low saturation of the perichondrium and cartilage regions indicated anisotropic and isotropic fiber orientations, respectively. Moreover, to quantify the orientation of collagen fibers, the local orientation histograms of all collagen fibers were summarized, and the orientation density of local angles was plotted in polar coordinates. The statistical results in Fig. 5E–H showed that the average fiber orientation of native perichondrium (Nperichondrium) and Eperichondrium was 6.31 ± 3.38° and 10.96 ± 6.87°, respectively ($P < 0.05$). The overall fiber orientation tended to be between −15° and 15°, and the proportions of Nperichondrium and Eperichondrium were 64.71 % and 56.91 %, respectively. The average fiber orientation of native cartilage (Ncartilage) and Ecartilage was 66.65 ± 17.99° and 63.62 ± 18.23°, respectively ($P > 0.05$), and the overall fiber orientation tended to be isotropic. Coherence is a measure of isotropic properties, ranging from 0 (when the image is isotropic in the analyzed region) to 1 (when the local structure has a dominant orientation). Nperichondrium (0.47 ± 0.06) had a higher degree of collagen fibril organization than Eperichondrium (0.28 ± 0.03) ($P < 0.001$), whereas the difference in the degree of collagen fibril organization between Ncartilage (0.08 ± 0.04) and Ecartilage (0.11 ± 0.03) was minimal ($P > 0.05$).

3.5. Similarities and differences between engineered and native tissues

The engineered and native tissues were processed for transcriptome analysis to observe their differences and similarities. Ncartilage, Nperichondrium, Ecartilage, and Eperichondrium have co-expressed and differentially expressed genes (Fig. 6A). The difference scatter plot, clustering heatmap, and Pearson's correlation heatmap revealed the differences and similarities between the groups, with the greatest differences between Ncartilage and Nperichondrium, and the highest similarities between Ecartilage and Eperichondrium (Fig. 6B–D). We speculated that this was because the Ecartilage and Eperichondrium had a uniform source of rabbit ear chondrocytes. Ecartilage more closely resembles Ncartilage than Eperichondrium, whereas Eperichondrium was more biased toward Nperichondrium than Ecartilage, suggesting that the Ecartilage tends to be oriented toward the cartilage, and the co-culture system in Eperichondrium has a tendency to be oriented toward the perichondrium. The next step was to characterize the differential information using GO and KEGG, which helped us understand the functional information of the differential genes in each group. Differentially expressed genes of the Ecartilage and Ncartilage were mainly enriched in functions related to migration, locomotion, localization, adhesion, communication, proliferation, and chondrogenic differentiation (Fig. 6E and F). The expression levels of chondrogenic-related genes (COL2A1, COL9A1, and COL9A2) and proliferation-related genes (FGF1 and FOS) in the Ecartilage were still lower than those in the Ncartilage (Fig. 6G), indicating that Ecartilage is almost similar to Ncartilage; however, further improvement is needed regarding cell behavior and

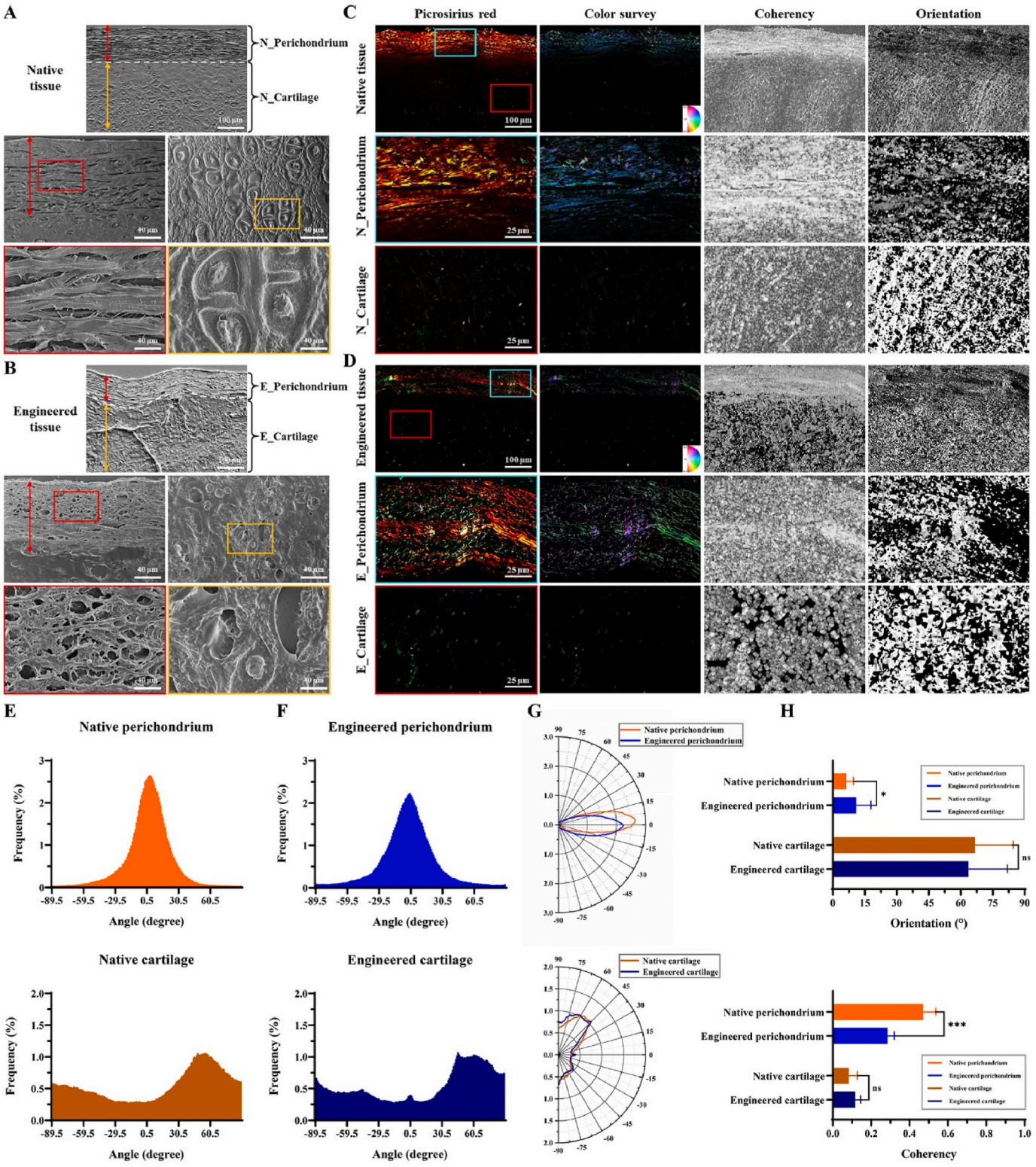

Fig. 5. Visualization and quantitative analysis of collagen fiber orientation. SEM images of the perichondrium layer and cartilage layer of (A) native tissue and (B) engineered tissue. Picrosirius Red staining and visualization images of the perichondrium layer and cartilage layer of (C) native tissue and (D) engineered tissue. (Color wheels: red/pink corresponds to fibers aligned towards 90° and cyan/blue corresponds to fibers oriented at 0°. Hue: Orientation. Saturation: Coherency.) Histograms of the local orientation in the perichondrium and cartilage layers of (E) native tissue and (F) engineered tissue. (G) Polar coordinate plots of local orientation density in the perichondrium layer and cartilage layers of native tissue and engineered tissue. (H) Statistical histograms of the orientation and coherency in the perichondrium and cartilage layers of native tissue and engineered tissue. Coherency (0–1): 0 (when the image is isotropic in the analyzed region) to 1 (when the local structure has a dominant orientation). $^{*}P < 0.05$. $^{***}P < 0.001$.

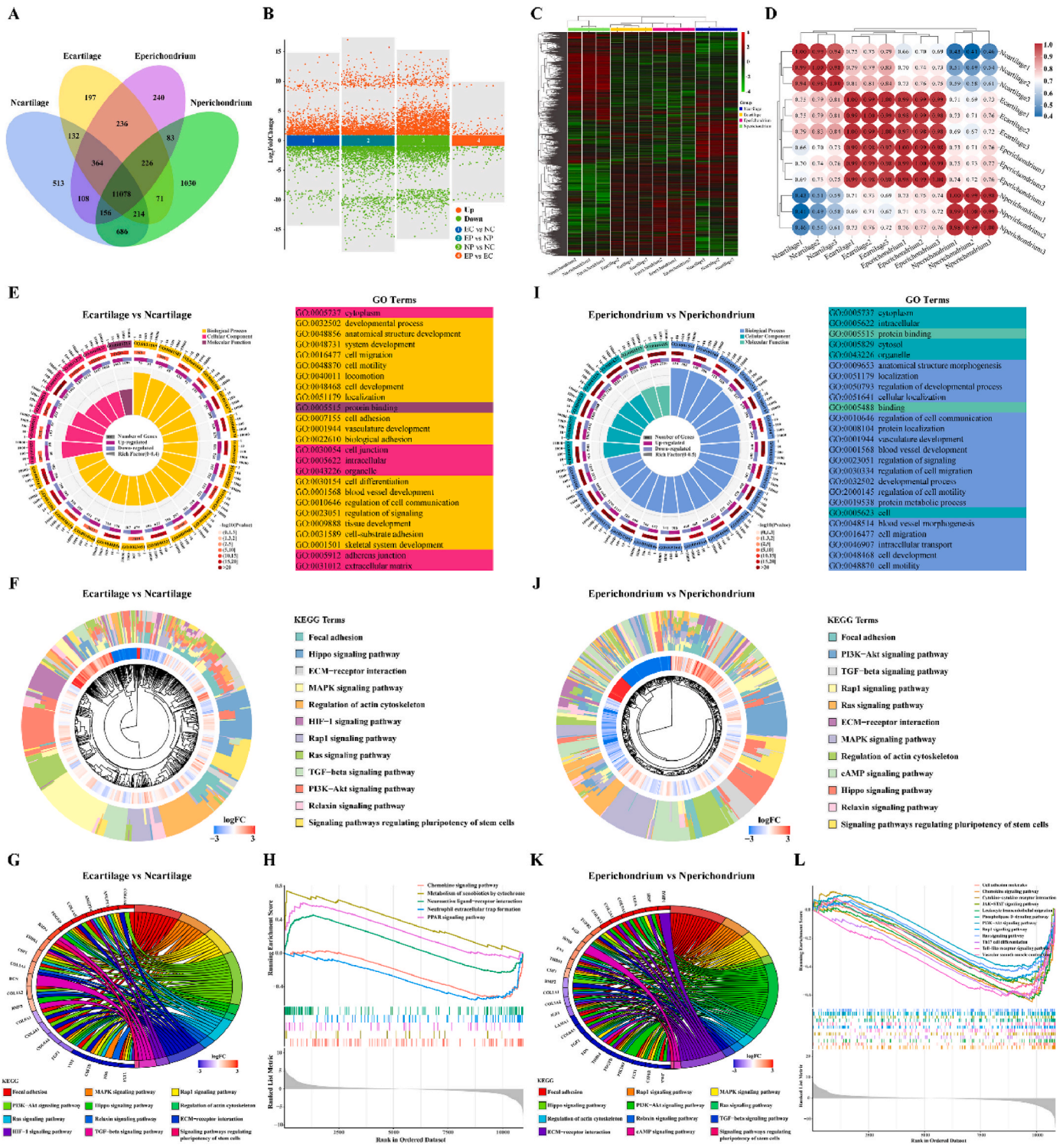

Fig. 6. Similarities and differences between engineered and native tissues. (A) Venn diagram, (B) Difference scatter plot (orange dots: FC > 2 and *P*-values <0.05; green dots: FC < 0.5 and *P*-values <0.05), (C) Clustering heatmap, and (D) Pearson's correlation heatmap (red represents high-correlation and blue represents low-correlation) of comparisons among Ncartilage, Nperichondrium, Ecartilage, and Eperichondrium. (E) GO enrichment circle diagram, (F) KEGG enrichment clustering diagram and (G) enrichment chord diagram, as well as (H) GSEA enrichment diagram of differential genes between Ecartilage and Ncartilage. (I) GO enrichment circle diagram, (J) KEGG enrichment clustering diagram and (K) enrichment chord diagram, as well as (L) GSEA enrichment diagram of differential genes between Eperichondrium and Nperichondrium.

matrix secretion ability. In addition, GSEA revealed the five most significant differential pathways (Fig. 6H), which were only related to immunity, suggesting that the Ecartilage was highly similar to Ncartilage, whereas the variability in immunity may be caused by the introduction of cells of different species. Similarly, Eperichondrium and Nperichondrium were subjected to GSEA, which showed that their differential genes were mainly enriched in functions related to adhesion, localization, communication, migration, proliferation, chondrogenesis, fibrogenesis, and vasculature development (Fig. 6I and J). The expression of genes related to cartilage development (COL2A1, COL9A1, and

SOX9) in the Eperichondrium was significantly higher than that in the Nperichondrium, whereas the expression of genes related to cell proliferation (FGF1, IGF1, and FOS), fibrogenesis (COL1A1, COL1A2, and COL6A5), and angiogenesis (VWF and FLT1) were lower than that in the Nperichondrium (Fig. 6K). In addition, GSEA suggested that the Eperichondrium was still deficient in adhesion, chemokines, proliferation, and angiogenesis compared with the Nperichondrium (Fig. 6L), indicating that the Eperichondrium needs to be further improved to be similar to the Nperichondrium in terms of cell behavior, fibrogenesis, and angiogenesis.

Next, the interaction between ADSC and chondrocytes in the co-culture system and their disparity with natural tissues needs clarification. The results of the comparison between the Nperichondrium and Ncartilage were used as a reference to clarify the discrepancy between the cartilage and perichondrium. Nperichondrium and Ncartilage had 12,134 co-expressed genes, with perichondrium-specific expression of 1410 genes and cartilage-specific expression of 1117 genes (Fig. 7A), and the upregulated genes in Ncartilage (including ACAN, COL2A1,

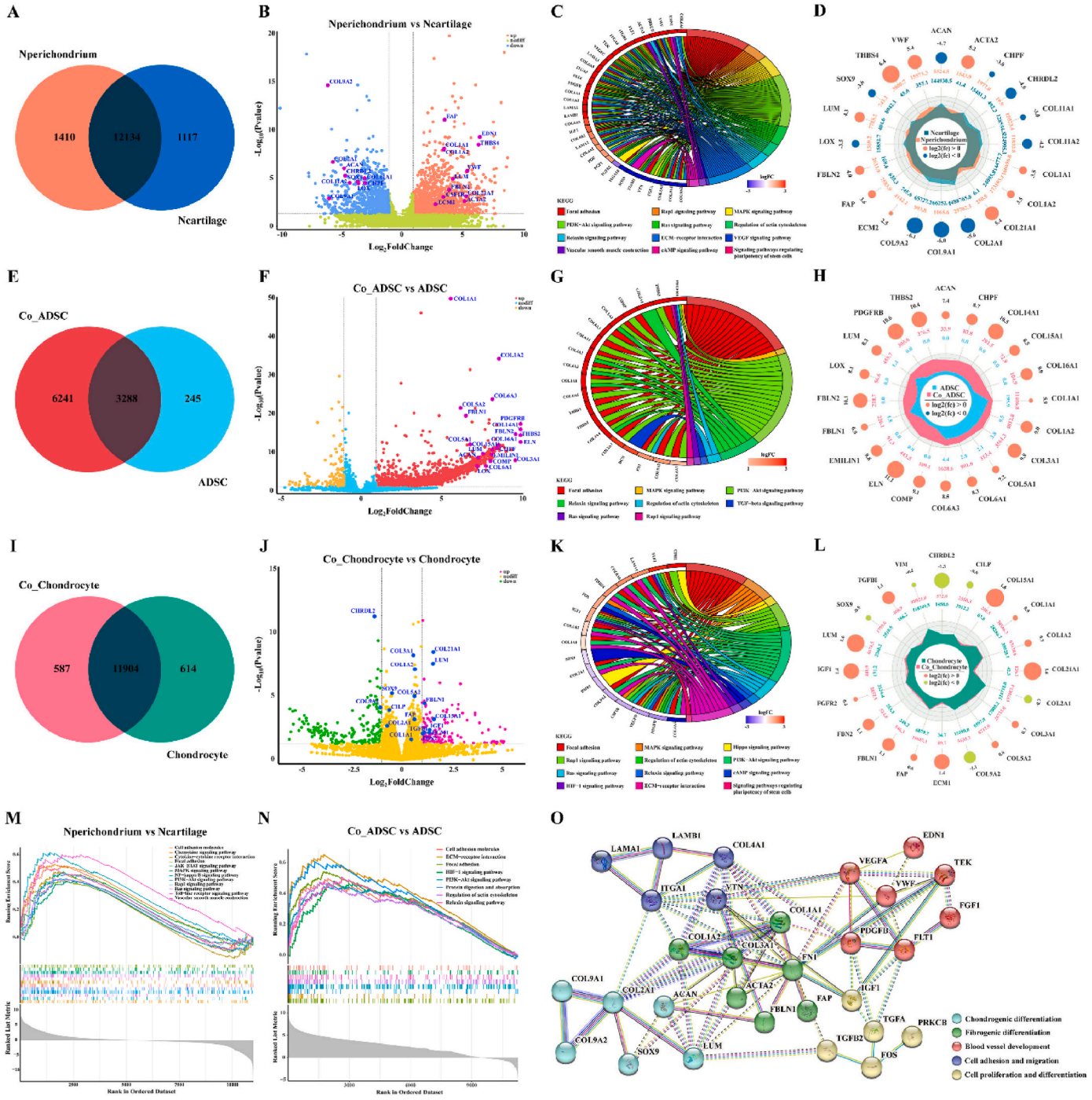

Fig. 7. Interaction between ADSC and chondrocytes in the co-culture system. (A) Venn diagram, (B) Volcano plot, (C) KEGG enrichment chord diagram, and (D) Radar plot of comparisons between Nperichondrium and Ncartilage. (E) Venn diagram, (F) Volcano plot, (G) KEGG enrichment chord diagram, and (H) Radar plot of comparisons between Co_ADSC and ADSC. (I) Venn diagram, (J) Volcano plot, (K) KEGG enrichment chord diagram, and (L) Radar plot of comparisons between Co_Chondrocyte and Chondrocyte. GSEA enrichment diagram of differential genes between (M) Nperichondrium and Ncartilage, (N) Co_ADSC and ADSC. (O) Interaction network of differential genes.

COL9A1, COL9A2, SOX9, and CHPF) were mainly associated with chondrogenesis, whereas the upregulated genes in Nperichondrium were mainly associated with fibrogenesis (including COL1A1, COL1A2, FAP, ACTA2, ECM, and FBLN2) and angiogenesis (including VWF, EDN1, and FLT1) (Fig. 7B). GO and KEGG analyses revealed that the differential genes were mainly enriched for adhesion, proliferation, ECM, fibrogenesis, chondrogenesis, and angiogenesis (Figs. S12A and B). The enrichment chord diagram further clarified that the major genes driving perichondrium and cartilage differences included cartilage ECM-related genes (including COL9A2, COL9A1, COL2A1, and SOX9), fibrogenesis-related genes (including COL1A1, COL1A2, COL4A1, and ACTA2), cell proliferation-related genes (IGF1, FGF1, and FOS), and angiogenesis-related genes (including EDN1, VWF, FLT1, TEK, and VEGF). Moreover, the expressions of related differential genes are revealed using a radar plot (Fig. 7C and D). When compared, co-ADSCs and ADSCs have 3288 co-expressed genes, with co-ADSCs and ADSCs specifically expressing 6241 and 245 genes, respectively (Fig. 7E). A volcano plot showed that chondrogenesis-related genes (including ACAN, CHPF, COMP, ELN, LOX, and EMILIN1) and fibrogenesis-related genes (including COL1A1, COL1A2, COL3A1, COL5A1, FBLN1, and FBLN2) were significantly upregulated in co-ADSCs after co-culturing with chondrocytes (Fig. 7F). GO and KEGG analyses showed that the differential genes were mainly enriched for adhesion, locomotion, communication, fibrogenesis, and chondrogenesis-related functions (Figs. S12C and D). The enrichment chordal diagram and radar plots revealed the differential genes and expression related to the above functions, indicating that the genes in co-ADSCs related to chondrogenesis (including COMP, COL2A1, and COL9A2) and fibrogenesis (including COL3A1, COL6A1, COL1A1, and FN1) were significantly higher than those in ADSCs (Fig. 7G and H). Meanwhile, the comparison of co-chondrocytes and chondrocytes revealed 11,904 co-expressed genes, with co-chondrocytes and chondrocytes specifically expressing 587 and 614 genes, respectively (Fig. 7I). A volcano plot showed a trend of downregulated chondrogenesis-related genes (including CHRDL2, COL9A2, SOX, CILP, and COL2A1) and upregulated fibrogenesis-related genes (including FBLN1, ECM1, FBN2, FAP, COL1A1, and COL3A1) in co-chondrocytes (Fig. 7J). GO and KEGG analyses revealed that the differential genes were mainly enriched in binding, migration, proliferation, ossification, fibrogenesis, and cartilage development-related functions (Figs. S12E and F), and the enrichment chordal diagram and radar plots clarified the key genes and their expression that drove co-chondrocyte transformation (Fig. 7K and L). In addition, functions related to adhesion, ECM, locomotion, chondrogenesis, and fibrogenesis were significantly enriched in co-ADSC, similar to those enriched in the Nperichondrium (Fig. 7M and N). Gene interaction network also revealed the interaction relationship of chondrogenic differentiation, fibrogenic differentiation, blood vessel development, cell adhesion and migration, and cell proliferation and differentiation in perichondrium and cartilage differential genes (Fig. 7O).

The results of the transcriptome sequencing were further verified using immunofluorescence and reverse transcription-polymerase chain reaction (RT-PCR). First, collagen I and II sources were confirmed using immunofluorescence (Fig. 8A). The results showed that there was a strong positive expression (red fluorescence) of the human nuclear antigen Lamin A/C in the Eperichondrium (the nuclei were long and spindle-shaped), and none in the Ecartilage (the nuclei were triangular and irregularly shaped), indicating that the implanted human ADSCs were maintained in the Eperichondrium and could survive for a long period, whereas the Ecartilage consisted mainly of implanted rabbit ear chondrocytes. The Eperichondrium showed a strong positive expression of collagen I (pink fluorescence) and a weak positive expression of collagen II (green fluorescence). Notably, the region with positive expression of collagen I largely overlapped with Lamin A/C (yellow arrow), indicating that collagen I in the Eperichondrium was secreted by the implanted human ADSCs. Meanwhile, there was a weak positive expression of collagen II around the Lamin A/C-positive region (as shown by the green arrows), whereas it was strongly positive in the Ecartilage, indicating that the rabbit ear chondrocytes implanted in the Eperichondrium not only expressed collagen II but also induced the expression of the implanted human ADSCs. However, due to the interaction within the co-culture system, the intensity of collagen II expression in the Eperichondrium was lower than that in the Ecartilage. In addition, RT-PCR analysis of the co-culture system (Fig. 8B) showed that co-ADSCs were affected by chondrocytes and had significantly higher expression of chondrogenesis-related genes (ACAN, COL2A1, COL9A1, ELN, and SOX9), fibrogenesis-related genes (COL1A1, COL3A1, FAP, FBN1, and ACTA2), and proliferation- and angiogenesis-related genes (FGF1, TGFB1, IGF1, VEGF, and VWF). In contrast, co-chondrocytes were affected by ADSCs (Fig. 8C), with significantly lower expression of chondrogenesis-related genes (ACAN, COL2A1, COL9A1, ELN, and SOX9) than the chondrocytes, and significantly higher expression of fibrogenesis-related genes and proliferation-related genes (COL1A1, COL3A1, FAP, FBN1, ACTA2, FGF1, and TGFB1), with no significant changes in angiogenesis-related genes (VEGF and VWF). These results illustrate that the main differences between Nperichondrium and Ncartilage are cartilage matrix secretion, fibrogenesis, and angiogenesis. Meanwhile, ADSCs and chondrocytes in the co-culture system interacted with each other, resulting in chondrocyte-induced chondrogenic and fibrogenic differentiation of co-ADSCs. ADSCs may induce chondrocyte dedifferentiation, resulting in the formation of functional perichondrium-like tissue. Therefore, the co-culture system allowed the Eperichondrium to combine chondrogenesis, fibrogenesis, and angiogenesis, which is more in line with the function of the natural perichondrium.

4. Discussion

The construction and regeneration of tissue-engineered auricles have always been pacesetters in tissue engineering, and have led to breakthroughs in clinical applications [9,41]. However, shrinkage and deformation caused by unstable regeneration quality and insufficient mechanical strength have majorly limited their popularity and application. The properties and strength of the auricle depend mainly on the ECM components and microstructure and the perichondrium coating [42]. The perichondrium contributes to the growth, structural stability, regeneration, and maintenance of the cartilage, and has the clinical potential to treat various cartilage-associated diseases and traumas. However, previous studies on the structural characteristics and the role of perichondrium are scarce. The parallel arrangement of type I collagen in the perichondrial matrix is associated with improved tensile strength, whereas the honeycomb network arrangement of type II collagen and elastin in the cartilage matrix contributes to improved compressive strength and stability. Therefore, defining the characteristics of microstructure is important in biomechanics. Accordingly, biomimetic materials and functional cells were controlled and assembled in an orderly manner using three-dimensional bioprinting technology to explore the effects of microgeometry on cell behavior and biomechanics. Finally, by simulating the matrix composition and microstructural features of the perichondrium and cartilage, an integrated biomimetic construction strategy for perichondrium-coated auricular cartilage was established to realize biomimicry in morphology, structure, and biomechanics, thereby improving mechanical properties and regeneration quality and promoting the clinical translation and application of tissue-engineered tissues or organs.

In the process of tissue regeneration, mimicking the structure of native tissues helps direct functional cells to form specific tissues [43,44]. The native auricle is lined by a stratified tissue called the perichondrium, which contributes to growth, structural stability, and regeneration and maintenance of the cartilage. Previous studies have shown that when the perichondrium on both sides of the auricular cartilage is intact, its extension and contraction are the same as the attached cartilage, and it maintains tight adhesion, while the auricular

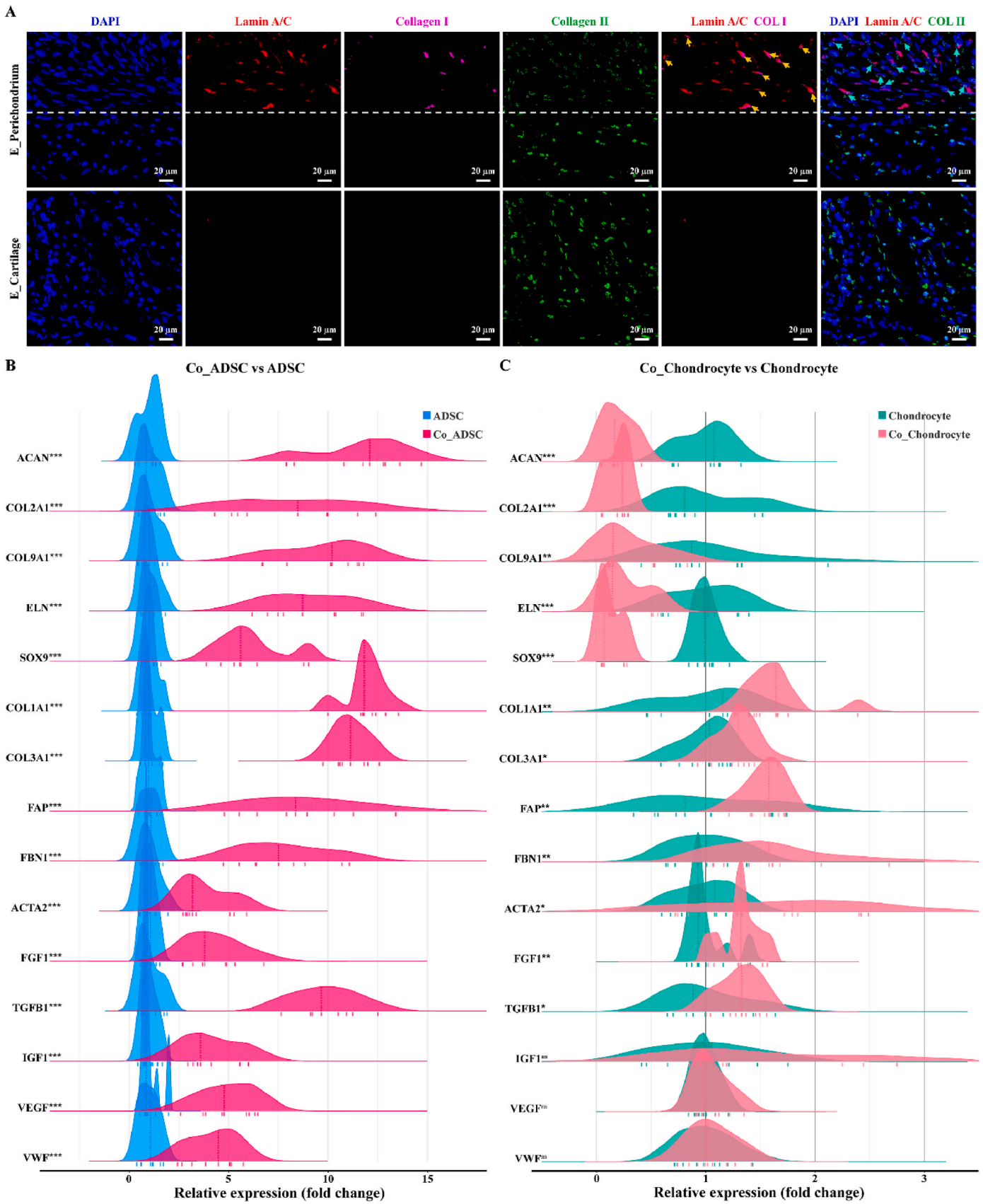

Fig. 8. Validation results of transcriptome analysis by immunofluorescence and RT-PCR. (A) Representative immunofluorescence images of engineered perichondrium-wrapped cartilage tissue with hierarchical structures. Ridgeline plots of gene expression differences between (B) Co_ADSC and ADSC, (C) Co_Chondrocyte and Chondrocyte. $^{*}P < 0.05$. $^{**}P < 0.01$. $^{***}P < 0.001$.

cartilage is easily broken when the perichondrium is removed [13]. Therefore, the flexibility of the auricular cartilage is largely provided by the perichondrium. However, the perichondrium and cartilage must be close enough to prevent displacement when external forces are applied to ensure the overall performance of the auricle. Previous studies have used freeze-dried porcine perichondrium which is pressed onto Ecartilage to improve its mechanical strength [42]. However, the perichondrium pressing method is not practical for constructing precisely shaped auricles and cannot realize a close combination of the perichondrium and cartilage. The collagen fibers of the perichondrium penetrate deeply into the cartilage matrix to form a complete structure, which has always been a barrier to tissue engineering. Previous studies have attempted to combine bioengineered skin with bioprinted cartilage for ear reconstruction, which is an effective method for tissue integration [45]. However, from the current clinical perspective, the use of skin expanders has greatly improved the regenerative effect of the skin, which is sufficient for auricular reconstructive surgery. Therefore, combining the perichondrium with the cartilage may be an appropriate method for tissue integration. In this study, a layered bioprinting strategy was proposed to realize the integrated construction of the perichondrium and cartilage. The preparation of a bioink with acellular cartilage matrix and gelatin as the main components can simulate the matrix components of the auricle and provide a bionic microenvironment for functional cells. Moreover, the application of natural materials reduces matrix degradation caused by inflammation to improve the mechanical properties of the ECM. Regarding printing methods, designing a parallel wave pattern for the perichondrium layer is beneficial for improving tensile strength, whereas designing a honeycomb pattern for the cartilage is conducive to improving compressive strength. Through the orientation and precise placement of the bioinks, the macroscopic structure and geometric configuration can be controlled to achieve structural bionics. In addition, the perichondrium is tightly attached to the cartilage, and collagen fibers protrude from the perichondrium and anchor to the cartilage matrix. To better simulate this structural feature, PEO is designed as a pore-forming agent that not only provides space for cells to proliferate and secrete matrix but also forms interlayer network traffic to assist perichondrium cells to grow into the cartilage layer and promote the tight connection between tissues [46,47].

To realize the above functions during structural reproduction, functional cells in the tissue must be mimicked. Many tissues and organs contain a certain number of progenitors or stem cells that can replace dead cells or restore tissues and organs after injury. There is evidence that perichondrium might contain chondrogenic progenitor cells, and mesenchymal-like cells originating from the perichondrium have been observed to proliferate actively and form a thick layer of cartilage matrix [48,49]. Perichondrium possible role as a microenvironment containing chondrocyte progenitor/stem cells (CSPCs). However, the number of perichondrium tissues is small, and the cell content is low, making it difficult to obtain sufficient seed cells. In some cases, chondroprogenitors were reported to fall under the minimal accepted criteria defining mesenchymal stromal cells (MSCs) and are thereby considered MSCs. ADSCs and CSPCs are stem cells with high similarity regarding marker expression and multidirectional differentiation abilities. Additionally, ADSCs have the advantages of abundance and reduced damage. More importantly, they regulate the balance of the immune response through a paracrine mechanism, promote the downregulation of the local inflammatory response, and improve the regeneration quality of the construct. Therefore, we used ADSCs co-cultured with auricular chondrocytes as functional cells in the perichondrium, whereas auricular chondrocytes were used as functional cells in the cartilage. Previous studies have confirmed that chondrocytes induce the differentiation of mesenchymal stem cells into chondrocytes by co-culturing or via cytokine activation and that the proportion of co-cultured cells affects the type of matrix component that is formed [50,51]. Therefore, ADSCs co-cultured with auricular chondrocytes, and auricular chondrocytes were used as seed cells from the bilateral perichondrium to the intermediate cartilage. A matrix gradient is formed with the help of a cell gradient to achieve bionic functional cells and ECM components.

Additionally, stimulation of cell proliferation and ECM synthesis during the formation of new cartilage is critical for the quality and clinical application of regenerated cartilage. Therefore, various growth factors such as basic fibroblast growth factor, insulin-like growth factor, and transforming growth factor can directly stimulate the proliferation of progenitor cells and/or immature chondrocytes and ECM synthesis in the early stages of new cartilage formation, which may help improve the quality of Ecartilage. In addition, mechanical stimulation is an effective promoter of ECM synthesis, and it improves mechanical properties [52]. Chondrocytes contain a complete set of mechanical sensors, including primary cilia, mechanically sensitive ion channels, integrins, and cytoskeletons, that sense and respond to various extracellular mechanical signals. Previous studies have confirmed that sustained mechanical stimulation can induce structural remodeling of the ECM, produce an anisotropic and mechanically robust structure, and improve the mechanical strength of Ecartilage. These properties cannot be achieved by using bioactive factors alone. Mechanical stimulation can promote nutrient exchange, maintain high cell vitality, and improve the regenerative quality of engineered tissue, enhancing its similarities to native tissue in terms of structure and function. Therefore, the routine addition of mechanical stimulation to the cell culture system may be an effective strategy for improving the quality of their engineered equivalents.

Although the perichondrium is an extremely thin structure in the auricle, it significantly contributes to the mechanical strength of the auricular cartilage. Cartilage with an intact perichondrium had a higher Young's modulus, lower relaxation slope, and lower relaxation level. Perichondrium-wrapped auricular cartilage has the advantage of viscoelasticity, making it more resistant to tensile and compressive forces. This may be related to the combined action of the perichondrium and cartilage. Under tension, the tendinous structure of the perichondrium and the tight connection between the perichondrium and cartilage can resist loads at both ends, thereby improving their overall load-bearing capacity. In the compressed state, the fibrous connection between the perichondrium and cartilage pulls toward the center, thus resisting the force that squeezes the surrounding cartilage. In this study, positive results were obtained by constructing a perichondrium-wrapped auricle with biomimetic hierarchical structures, which improved the viability and biomechanical properties of the auricle grafts. However, the mechanisms underlying need to be verified in future studies. Additionally, different locations of the auricle may have different requirements for the thickness and direction of the collagen fibers in the perichondrium and cartilage, which needs to be resolved in further construction of auricle tissue. Ignoring this may be counterproductive for maintaining the shape of the auricle because inappropriate perichondrial tension may damage the auricular structure. Currently, the reconstructed auricle substitutes were not comparable to the native auricle. In future research, it will be necessary to introduce exogenous growth factors to promote cartilage regeneration and introduce a dynamic bioreactor, such as hydrostatic pressure, perfusion system, and shear forces, to further improve regenerative quality and mechanical properties. This will require multidisciplinary effort and close cooperation between Materials, Engineering, Medicine, and other interdisciplinary fields.

5. Conclusion

To improve the regeneration quality and mechanical properties of tissue-engineered auricles, this study presents a novel strategy for the integrated construction of bioengineered perichondrium with bioprinted cartilage with hierarchical structures for auricular reconstruction. By simulating the matrix composition and microstructure characteristics of the native auricle, biomimetic materials and functional cells were controlled and assembled in an orderly manner using three-dimensional bioprinting, and auricular equivalents with bilateral

perichondrium and intermediate cartilage were successfully fabricated and regenerated. These equivalents mimicked the native auricles in terms of morphology, structure, and biomechanics, and inspired improvements in the viability and biomechanical properties of engineered auricles. Although the reconstructed auricle substitutes were still not comparable to the native auricle and required further close cooperation among multiple disciplines, the current multi-level and multi-scale biomimetic construction strategy can provide a technical reference for the integrated construction of complex tissues to promote the clinical translation and application of engineered tissues.

CRediT authorship contribution statement

Litao Jia: Writing – original draft, Visualization, Methodology, Investigation, Data curation, Conceptualization. **Siyu Liu:** Visualization, Conceptualization. **Luosha Gu:** Investigation, Data curation. **Xiaomin Liu:** Data curation. **Kexin Sun:** Methodology, Investigation, Data curation. **Feiyang Chu:** Methodology, Data curation. **Jinshi Zeng:** Data curation. **Wenshuai Liu:** Methodology, Conceptualization. **Haiyue Jiang:** Writing – review & editing, Supervision, Conceptualization. **Xia Liu:** Writing – review & editing, Supervision, Methodology, Conceptualization.

Ethics approval and consent to participate

Animal experiments were approved by the Animal Care and Experiment Committee of the Plastic Surgery Hospital (Institute), Chinese Academy of Medical Sciences and Peking Union Medical College (Approval No. 2023-86).

Declaration of competing interest

The authors declare that they have no known competing financial interests or personal relationships that could have appeared to influence the work reported in this paper.

Acknowledgments

This work was supported by the National Key R&D Program of China (Grant No. 2024YFA1107800), the Chinese Academy of Medical Sciences Innovation Fund for Medical Sciences (2021-I2M-1–052), the National Natural Science Foundation of China (82371796), the Beijing Natural Science Foundation (7244400), and the Fundamental Research Funds for the Central Universities (3332024056).

Appendix A. Supplementary data

Supplementary data to this article can be found online at https://doi.org/10.1016/j.bioactmat.2025.02.011.

References

[1] D.V. Luquetti, C.L. Heike, A.V. Hing, M.L. Cunningham, T.C. Cox, Microtia: epidemiology and genetics, Am. J. Med. Genet. 158A (1) (2012) 124–139, https://doi.org/10.1002/ajmg.a.34352.
[2] D.V. Luquetti, E. Leoncini, P. Mastroiacovo, Microtia-anotia: a global review of prevalence rates, Birth Defects Res A Clin Mol Teratol 91 (9) (2011) 813–822, https://doi.org/10.1002/bdra.20836.
[3] R.A. Bly, A.D. Bhrany, C.S. Murakami, K.C. Sie, Microtia reconstruction, Facial Plast Surg Clin North Am 24 (4) (2016) 577–591, https://doi.org/10.1016/j.fsc.2016.06.011.
[4] R.C. Tanzer, Total reconstruction of the external ear, Plast. Reconstr. Surg. 23 (1) (1959) 1–15, https://doi.org/10.1097/00006534-195901000-00001.
[5] Z. Xu, T. Li, R. Zhang, Q. Zhang, F. Xu, D. Li, Y. Li, X. Chen, Strategies for the treatment of auricular complications after the first stage of autologous cartilage microtia reconstruction, Plast. Reconstr. Surg. 150 (1) (2022) 157e–167e, https://doi.org/10.1097/PRS.0000000000009257.
[6] E.M. Ronde, M. Esposito, Y. Lin, F.S. van Etten-Jamaludin, N.W. Bulstrode, C. C. Breugem, Long-term complications of microtia reconstruction: a systematic review, J Plast Reconstr Aesthet Surg 74 (12) (2021) 3235–3250, https://doi.org/10.1016/j.bjps.2021.08.001.
[7] L. Nayyer, K.H. Patel, A. Esmaeili, R.A. Rippel, M. Birchall, G. O'Toole, P.E. Butler, A.M. Seifalian, Tissue engineering: revolution and challenge in auricular cartilage reconstruction, Plast. Reconstr. Surg. 129 (5) (2012) 1123–1137, https://doi.org/10.1097/PRS.0b013e31824a2c1c.
[8] D.A. Bichara, N.A. O'Sullivan, I. Pomerantseva, X. Zhao, C.A. Sundback, J. P. Vacanti, M.A. Randolph, The tissue-engineered auricle: past, present, and future, Tissue Eng Part B Rev 18 (1) (2012) 51–61, https://doi.org/10.1089/ten.TEB.2011.0326.
[9] G. Zhou, H. Jiang, Z. Yin, Y. Liu, Q. Zhang, C. Zhang, B. Pan, J. Zhou, X. Zhou, H. Sun, D. Li, A. He, Z. Zhang, W. Zhang, W. Liu, Y. Cao, In vitro regeneration of patient-specific ear-shaped cartilage and its first clinical application for auricular reconstruction, EBioMedicine 28 (2018) 287–302, https://doi.org/10.1016/j.ebiom.2018.01.011.
[10] Y. Cao, J.P. Vacanti, K.T. Paige, J. Upton, C.A. Vacanti, Transplantation of chondrocytes utilizing a polymer-cell construct to produce tissue-engineered cartilage in the shape of a human ear, Plast. Reconstr. Surg. 100 (2) (1997) 297–302, https://doi.org/10.1097/00006534-199708000-00001. ; discussion 3-4.
[11] L. Nimeskern, G.J. van Osch, R. Muller, K.S. Stok, Quantitative evaluation of mechanical properties in tissue-engineered auricular cartilage, Tissue Eng Part B Rev 20 (1) (2014) 17–27, https://doi.org/10.1089/ten.TEB.2013.0117.
[12] H.P. Lee, L. Gu, D.J. Mooney, M.E. Levenston, O. Chaudhuri, Mechanical confinement regulates cartilage matrix formation by chondrocytes, Nat. Mater. 16 (12) (2017) 1243–1251, https://doi.org/10.1038/nmat4993.
[13] D. Gvaramia, J. Kern, Y. Jakob, M. Zenobi-Wong, N. Rotter, Regenerative potential of perichondrium: a tissue engineering perspective, Tissue Engineering Part B: Reviews 28 (3) (2022) 531–541, https://doi.org/10.1089/ten.teb.2021.0054.
[14] H. Sun, J. Zhou, Q. Wang, H. Jiang, Q. Yang, Contribution of perichondrium to the mechanical properties of auricular cartilage, J. Biomech. 126 (2021) 110638, https://doi.org/10.1016/j.jbiomech.2021.110638.
[15] E. Zucchelli, M. Birchall, N.W. Bulstrode, P. Ferretti, Modeling normal and pathological ear cartilage in vitro using somatic stem cells in three-dimensional culture, Front. Cell Dev. Biol. 8 (2020) 666, https://doi.org/10.3389/fcell.2020.00666.
[16] Y. Shi, R. Guo, Q. Hou, H. Hu, H. Wang, H. Jiang, The effect of perichondrium on biological and biomechanical properties of molded diced cartilage grafts, Aesthetic Plast. Surg. 44 (2) (2020) 549–557, https://doi.org/10.1007/s00266-019-01581-5.
[17] J.M. Bliley, D.J. Shiwarski, A.W. Feinberg, 3D-bioprinted human tissue and the path toward clinical translation, Sci. Transl. Med. 14 (666) (2022) eabo7047, https://doi.org/10.1126/scitranslmed.abo7047.
[18] A.C. Daly, M.E. Prendergast, A.J. Hughes, J.A. Burdick, Bioprinting for the biologist, Cell 184 (1) (2021) 18–32, https://doi.org/10.1016/j.cell.2020.12.002.
[19] L. Ouyang, Pushing the rheological and mechanical boundaries of extrusion-based 3D bioprinting, Trends Biotechnol. 40 (7) (2022) 891–902, https://doi.org/10.1016/j.tibtech.2022.01.001.
[20] Z. Jin, Y. Li, K. Yu, L. Liu, J. Fu, X. Yao, A. Zhang, Y. He, 3D printing of physical organ models: recent developments and challenges, Adv. Sci. 8 (17) (2021) e2101394, https://doi.org/10.1002/advs.202101394.
[21] L. Jia, Y. Hua, J. Zeng, W. Liu, D. Wang, G. Zhou, X. Liu, H. Jiang, Bioprinting and regeneration of auricular cartilage using a bioactive bioink based on microporous photocrosslinkable acellular cartilage matrix, Bioact. Mater. 16 (2022) 66–81, https://doi.org/10.1016/j.bioactmat.2022.02.032.
[22] P. Fisch, N. Broguiere, S. Finkielsztein, T. Linder, M. Zenobi-Wong, Bioprinting of cartilaginous auricular constructs utilizing an enzymatically crosslinkable bioink, Adv. Funct. Mater. 31 (16) (2021), https://doi.org/10.1002/adfm.202008261.
[23] L. Jia, Y. Zhang, L. Yao, P. Zhang, Z. Ci, W. Zhang, C. Miao, X. Liang, A. He, Y. Liu, S. Tang, R. Zhang, X. Wang, Y. Cao, G. Zhou, Regeneration of human-ear-shaped cartilage with acellular cartilage matrix-based biomimetic scaffolds, Appl. Mater. Today 20 (2020) 100639, https://doi.org/10.1016/j.apmt.2020.100639.
[24] P.M. Crapo, T.W. Gilbert, S.F. Badylak, An overview of tissue and whole organ decellularization processes, Biomaterials 32 (12) (2011) 3233–3243, https://doi.org/10.1016/j.biomaterials.2011.01.057.
[25] Y. Hua, Y. Huo, B. Bai, J. Hao, G. Hu, Z. Ci, X. Wu, M. Yu, X. Wang, H. Chen, W. Ren, Y. Zhang, X. Wang, G. Zhou, Fabrication of biphasic cartilage-bone integrated scaffolds based on tissue-specific photo-crosslinkable acellular matrix hydrogels, Mater Today Bio 17 (2022) 100489, https://doi.org/10.1016/j.mtbio.2022.100489.
[26] J. Chen, J. Yang, L. Wang, X. Zhang, B.C. Heng, D.A. Wang, Z. Ge, Modified hyaluronic acid hydrogels with chemical groups that facilitate adhesion to host tissues enhance cartilage regeneration, Bioact. Mater. 6 (6) (2021) 1689–1698, https://doi.org/10.1016/j.bioactmat.2020.11.020.
[27] Y. Liu, G. Dzidotor, T.T. Le, T. Vinikoor, K. Morgan, E.J. Curry, R. Das, A. McClinton, E. Eisenberg, L.N. Apuzzo, K.T.M. Tran, P. Prasad, T.J. Flanagan, S. W. Lee, H.M. Kan, M.T. Chorsi, K.W.H. Lo, C.T. Laurencin, T.D. Nguyen, Exercise-induced piezoelectric stimulation for cartilage regeneration in rabbits, Sci. Transl. Med. 14 (627) (2022) eabi7282, https://doi.org/10.1126/scitranslmed.abi7282.
[28] M. Hou, B. Tian, B. Bai, Z. Ci, Y. Liu, Y. Zhang, G. Zhou, Y. Cao, Dominant role of in situ native cartilage niche for determining the cartilage type regenerated by BMSCs, Bioact. Mater. 13 (2022) 149–160, https://doi.org/10.1016/j.bioactmat.2021.11.007.
[29] Y. Xu, L. Duan, Y. Li, Y. She, J. Zhu, G. Zhou, G. Jiang, Y. Yang, Nanofibrillar decellularized wharton's jelly matrix for segmental tracheal repair, Adv. Funct. Mater. 30 (14) (2020) 1910067, https://doi.org/10.1002/adfm.201910067.

[30] F. Zeng, Z. Chen, R. Chen, W.J. Shufesky, M. Bandyopadhyay, G. Camirand, M. H. Oberbarnscheidt, M.L.G. Sullivan, C.J. Baty, M.Q. Yang, M. Calderon, D.B. Stolz, G. Erdos, R. Pelanda, T.V. Brennan, S.D. Catz, S.C. Watkins, A.T. Larregina, A. E. Morelli, Graft-derived extracellular vesicles transported across subcapsular sinus macrophages elicit B cell alloimmunity after transplantation, Sci. Transl. Med. 13 (585) (2021), https://doi.org/10.1126/scitranslmed.abb0122.
[31] Y. Huang, G. Hu, C. Ji, H. Xiong, Glass-cutting medical images via a mechanical image segmentation method based on crack propagation, Nat. Commun. 11 (1) (2020) 5669, https://doi.org/10.1038/s41467-020-19392-7.
[32] E.T. Pashuck, M. Stevens, From clinical imaging to implantation of 3D printed tissues, Nat. Biotechnol. 34 (3) (2016) 295–296, https://doi.org/10.1038/nbt.3503.
[33] Y. Liu, L. Zhang, G. Zhou, Q. Li, W. Liu, Z. Yu, X. Luo, T. Jiang, W. Zhang, Y. Cao, In vitro engineering of human ear-shaped cartilage assisted with CAD/CAM technology, Biomaterials 31 (8) (2010) 2176–2183, https://doi.org/10.1016/j.biomaterials.2009.11.080.
[34] A. Schwab, R. Levato, M. D'Este, S. Piluso, D. Eglin, J. Malda, Printability and shape fidelity of bioinks in 3D bioprinting, Chem Rev 120 (19) (2020) 11028–11055, https://doi.org/10.1021/acs.chemrev.0c00084.
[35] S. Van Belleghem, L. Torres Jr., M. Santoro, B. Mahadik, A. Wolfand, P. Kofinas, J. P. Fisher, Hybrid 3D printing of synthetic and cell-laden bioinks for shape retaining soft tissue grafts, Adv. Funct. Mater. 30 (3) (2020), https://doi.org/10.1002/adfm.201907145.
[36] Z. Yin, D. Li, Y. Liu, S. Feng, L. Yao, X. Liang, C. Miao, Y. Xu, M. Hou, R. Zhang, W. Zhang, W. Liu, Y. Liu, G. Zhou, Y. Cao, Regeneration of elastic cartilage with accurate human-ear shape based on PCL strengthened biodegradable scaffold and expanded microtia chondrocytes, Appl. Mater. Today 20 (2020), https://doi.org/10.1016/j.apmt.2020.100724.
[37] W. Dai, L. Zhang, Y. Yu, W. Yan, F. Zhao, Y. Fan, C. Cao, Q. Cai, X. Hu, Y. Ao, 3D bioprinting of heterogeneous constructs providing tissue-specific microenvironment based on host–guest modulated dynamic hydrogel bioink for osteochondral regeneration, Adv. Funct. Mater. 32 (23) (2022), https://doi.org/10.1002/adfm.202200710.
[38] A. Dufour, X.B. Gallostra, C. O'Keeffe, K. Eichholz, S. Von Euw, O. Garcia, D. J. Kelly, Integrating melt electrowriting and inkjet bioprinting for engineering structurally organized articular cartilage, Biomaterials 283 (2022) 121405, https://doi.org/10.1016/j.biomaterials.2022.121405.
[39] Y. Hua, H. Xia, L. Jia, J. Zhao, D. Zhao, X. Yan, Y. Zhang, S. Tang, G. Zhou, L. Zhu, Q. Lin, Ultrafast, tough, and adhesive hydrogel based on hybrid photocrosslinking for articular cartilage repair in water-filled arthroscopy, Sci. Adv. 7 (35) (2021) eabg0628, https://doi.org/10.1126/sciadv.abg0628.
[40] C. Ji, M. Qiu, H. Ruan, C. Li, L. Cheng, J. Wang, C. Li, J. Qi, W. Cui, L. Deng, Transcriptome analysis revealed the symbiosis niche of 3D scaffolds to accelerate bone defect healing, Adv. Sci. 9 (8) (2022) e2105194, https://doi.org/10.1002/advs.202105194.
[41] N. Bhamare, K. Tardalkar, A. Khadilkar, P. Parulekar, M.G. Joshi, Tissue engineering of human ear pinna, Cell Tissue Bank. 23 (3) (2022) 441–457, https://doi.org/10.1007/s10561-022-09991-7.
[42] J.W. Xu, T.S. Johnson, P.M. Motarjem, G.M. Peretti, M.A. Randolph, M. J. Yaremchuk, Tissue-engineered flexible ear-shaped cartilage, Plast. Reconstr. Surg. 115 (6) (2005) 1633–1641, https://doi.org/10.1097/01.prs.0000161465.21513.5d.
[43] O.J. Pundel, L.M. Blowes, J.T. Connelly, Extracellular adhesive cues physically define nucleolar structure and function, Adv. Sci. 9 (10) (2022) e2105545, https://doi.org/10.1002/advs.202105545.
[44] Y. Sun, Y. You, W. Jiang, B. Wang, Q. Wu, K. Dai, 3D bioprinting dual-factor releasing and gradient-structured constructs ready to implant for anisotropic cartilage regeneration, Sci. Adv. 6 (37) (2020), https://doi.org/10.1126/sciadv.aay1422.
[45] D. Zielinska, P. Fisch, U. Moehrlen, S. Finkielsztein, T. Linder, M. Zenobi-Wong, T. Biedermann, A.S. Klar, Combining bioengineered human skin with bioprinted cartilage for ear reconstruction, Sci. Adv. 9 (40) (2023), https://doi.org/10.1126/sciadv.adh1890.
[46] S. Yi, Q. Liu, Z. Luo, J.J. He, H.L. Ma, W. Li, D. Wang, C. Zhou, C.E. Garciamendez, L. Hou, J. Zhang, Y.S. Zhang, Micropore-forming gelatin methacryloyl (GelMA) bioink toolbox 2.0: designable tunability and adaptability for 3D bioprinting applications, Small 18 (25) (2022) e2106357, https://doi.org/10.1002/smll.202106357.
[47] G. Ying, N. Jiang, C. Parra, G. Tang, J. Zhang, H. Wang, S. Chen, N.P. Huang, J. Xie, Y.S. Zhang, Bioprinted injectable hierarchically porous gelatin methacryloyl hydrogel constructs with shape-memory properties, Adv. Funct. Mater. 30 (46) (2020), https://doi.org/10.1002/adfm.202003740.
[48] J. Ma, Y. Zhang, Z. Yan, P. Wu, C. Li, R. Yang, X. Lu, X. Chen, A. He, Y. Fu, D. Ma, W. Tian, T. Zhang, Single-cell transcriptomics reveals pathogenic dysregulation of previously unrecognised chondral stem/progenitor cells in children with microtia, Clin. Transl. Med. 12 (2) (2022) e702, https://doi.org/10.1002/ctm2.702.
[49] X. Zhang, L. Qi, Y. Chen, Z. Xiong, J. Li, P. Xu, Z. Pan, H. Zhang, Z. Chen, K. Xue, K. Liu, The in vivo chondrogenesis of cartilage stem/progenitor cells from auricular cartilage and the perichondrium, Am J Transl Res 11 (5) (2019) 2855–2865. https://www.ncbi.nlm.nih.gov/pubmed/31217859.
[50] L. Zhang, A. He, Z. Yin, Z. Yu, X. Luo, W. Liu, W. Zhang, Y. Cao, Y. Liu, G. Zhou, Regeneration of human-ear-shaped cartilage by co-culturing human microtia chondrocytes with BMSCs, Biomaterials 35 (18) (2014) 4878–4887, https://doi.org/10.1016/j.biomaterials.2014.02.043.
[51] X. Liu, H. Sun, D. Yan, L. Zhang, X. Lv, T. Liu, W. Zhang, W. Liu, Y. Cao, G. Zhou, In vivo ectopic chondrogenesis of BMSCs directed by mature chondrocytes, Biomaterials 31 (36) (2010) 9406–9414, https://doi.org/10.1016/j.biomaterials.2010.08.052.
[52] B. Yang, K. Wei, C. Loebel, K. Zhang, Q. Feng, R. Li, S.H.D. Wong, X. Xu, C. Lau, X. Chen, P. Zhao, C. Yin, J.A. Burdick, Y. Wang, L. Bian, Enhanced mechanosensing of cells in synthetic 3D matrix with controlled biophysical dynamics, Nat. Commun. 12 (1) (2021) 3514, https://doi.org/10.1038/s41467-021-23120-0.